

An optimisation–based domain–decomposition reduced order model for the incompressible Navier-Stokes equations

Ivan Prusak^{*a}, Monica Nonino^{†b}, Davide Torlo^{‡a}, Francesco Ballarin^{§c},
and Gianluigi Rozza^{¶a}

^aMathematics Area, mathLab, SISSA, 34136 Trieste, Italy

^bFakultät für Mathematik, Universität Wien, 1090 Wien, Austria

^cDepartment of Mathematics and Physics, Università Cattolica del
Sacro Cuore, 25133 Brescia, Italy,

Abstract

The aim of this work is to present a model reduction technique in the framework of optimal control problems for partial differential equations. We combine two approaches used for reducing the computational cost of the mathematical numerical models: domain–decomposition (DD) methods and reduced–order modelling (ROM). In particular, we consider an optimisation–based domain–decomposition algorithm for the parameter–dependent stationary incompressible Navier–Stokes equations. Firstly, the problem is described on the subdomains coupled at the interface and solved through an optimal control problem, which leads to the complete separation of the subdomain problems in the DD method. On top of that, a reduced model for the obtained optimal–control problem is built; the procedure is based on the Proper Orthogonal Decomposition technique and a further Galerkin projection. The presented methodology is tested on two fluid dynamics benchmarks: the stationary backward–facing step and lid-driven cavity flow. The numerical tests show a significant reduction of the computational costs in terms of both the problem dimensions and the number of optimisation iterations in the domain–decomposition algorithm.

Keywords: domain decomposition, optimal control, reduced order modelling, computational fluid dynamics, Proper Orthogonal Decomposition

*iprusak@sissa.it

†monica.nonino@univie.ac.at

‡dtorlo@sissa.it

§francesco.ballarin@unicatt.it

¶grozza@sissa.it

1 Introduction

In the last decades, there has been a growing interest in approximation techniques for partial differential equations (PDEs) that exploit high-performance computing within different fields of applications: industrial applications, naval engineering, aeronautics engineering, medical engineering, etc. Very often these problems have prohibitively high computational costs, and there is always the need of much more effective algorithms in order to alleviate the complexities of numerical models.

Two of the most investigated and most important topics for rendering low computational costs are the reduced-order modelling for parameter-dependent PDEs [22] and domain-decomposition algorithms [32]. In the former case, equations of interest usually depend on a given set of parameters; these parameters can describe either the physical properties of the sought quantities or the geometrical configuration of the physical domain over which the problem is posed. Model-order reduction is a technique based on the effective decoupling of the computationally expensive off-line and usually computationally cheap online phase which provides a solution for any parameter value: for details we refer to [22]. Model order reduction has been successfully employed in different fields such as fluid dynamics [3, 9, 11, 13, 28, 33, 35, 36, 37, 38, 39, 41] and structural mechanics [6, 7, 21, 34, 40, 43]. Among the aforementioned applications a significant type of problems often emerges, namely saddle-point problems [8, 15], for which special care has to be taken in order to construct stable pairs of the reduced spaces; in particular, in fluid dynamics problems this is achieved by introducing so-called velocity supremisers, see, for instance, [5, 15, 28, 42].

Another very efficient way for reducing the computational complexity of numerical modes is Domain Decomposition (DD) method. Any domain decomposition method is based on the assumption that a given physical domain of interest is partitioned into subdomains; the original problem is then recast upon each subdomain yielding a family of subproblems of reduced size that are coupled to one another through the values and fluxes of the unknown solution at the subdomain interfaces [31, 32]. Very often the interface coupling is relaxed at the expense of providing an iterative process among subdomains, allowing a split of each of the subdomain solvers and making it computationally feasible. Domain decomposition methods can be extremely advantageous in the case of very complex geometries as well as in the case of multi-physics problems. The latter is even more attractive if we consider that there are often available state-of-the-art codes for a subcomponent model of a multi-physics problem which can be effectively exploited by decoupling algorithms; see, for instance, [14, 16, 24, 27].

In this paper, we bring our attention to domain-decomposition methods using an optimisation approach to ensure the coupling of the interface conditions between subdomains as it is presented, for example, in [20, 17]. In particular, we exploit both aforementioned techniques: optimisation-based domain decomposition algorithm in combination with projection-based reduced-order models. This paper is the first step towards the development of an efficient reduced-order model for an optimisation-based domain-decomposition algorithm for Fluid-Structure Interaction (FSI) problems [6]. It is even more attractive in the view of the articles [25, 26] where the authors are suggesting that this approach leads to a stable segregated model for FSI problems in the case of added-mass effect [10]; we also mention here some already successful ROM results in developing stable semi-implicit partitioned approaches, e.g., [4, 29, 30].

Very recently, authors of the paper [12] have introduced a novel partitioned approach for ROMs, where they couple either two different reduced-order models on each subdomain or a reduced-order model on one subdomain and a full-order (Finite Element) model on the other for the case of nonstationary diffusion-advection problems. In this context, the construction followed in this paper could be also applicable to the coupling presented in [12], as long as there is a way of casting functions defined on the subdomain interface onto the approximation spaces

used on the corresponding subdomains; this will be subject of future work.

As mentioned before, the use of optimisation-based domain-decomposition methods for PDEs goes as back as the end of the 1990s, e.g., [18]. It had been successfully studied in the case of Navier–Stokes equations as well, see [20]. As for the novelty of this work, to the best of the authors’ knowledge, this is the first attempt of combining the aforementioned technique with projection-based Reduced Order Models in order to provide a computationally efficient algorithm for parametrised PDEs.

A possible extension of current work could be the application of the technique described in this paper to optimal-control problems; in this case, as, for example, in [18], we have to deal with multi-objective optimisation problems - one for the optimal control and another one for the domain-decomposition part.

This work is outlined as follows. In Section 2 we introduce the monolithic and the optimisation-based domain-decomposition formulation of the incompressible Navier–Stokes equations in both strong and weak forms. Furthermore, we derive the optimality condition for the resulting optimal control problem and compute the expression for the gradient of the objective functional. Section 3 lists a gradient-based optimisation algorithm for the problem derived in the previous section. In section 4 we describe the Finite Element discretisation of the problem of interest and provide a finite-dimensional high-fidelity optimisation problem. Section 5 deals with the reduced-order model which is based on a reduced basis generation by Proper Orthogonal Decomposition methodology and the Galerkin projection of the high-fidelity problem onto the lower-dimensional reduced spaces. In Section 6 we show some numerical results for two toy problems: the backward-facing step and the lid-driven cavity flows. Conclusions will follow in Section 7.

2 Problem formulation

In this section, starting with a monolithic formulation of the incompressible Navier-Stokes equations we introduce a two-domain optimisation-based domain-decomposition formulation in both strong and weak forms. Then, the optimality conditions of the resulting optimal control problem are derived followed by the expression of the gradient of the objective functional obtained by sensitivity analysis.

2.1 Monolithic formulation

Let Ω be a physical domain of interest: we assume Ω to be an open subset of \mathbb{R}^2 and Γ to be the boundary of Ω . Let $f : \Omega \rightarrow \mathbb{R}^2$ be the forcing term, ν the kinematic viscosity, u_D a given Dirichlet datum. The problem reads as follows: find the velocity field $u : \Omega \rightarrow \mathbb{R}^2$ and the pressure $p : \Omega \rightarrow \mathbb{R}$ s.t.

$$-\nu\Delta u + (u \cdot \nabla) u + \nabla p = f \quad \text{in } \Omega, \tag{1a}$$

$$-\text{div} u = 0 \quad \text{in } \Omega, \tag{1b}$$

$$u = u_D \quad \text{on } \Gamma_D, \tag{1c}$$

$$\nu \frac{\partial u}{\partial n} - pn = 0 \quad \text{on } \Gamma_N, \tag{1d}$$

where Γ_D and Γ_N are disjoint subsets of Γ (as it is shown in Figure 1) and n is an outward unit normal vector to Γ_N .

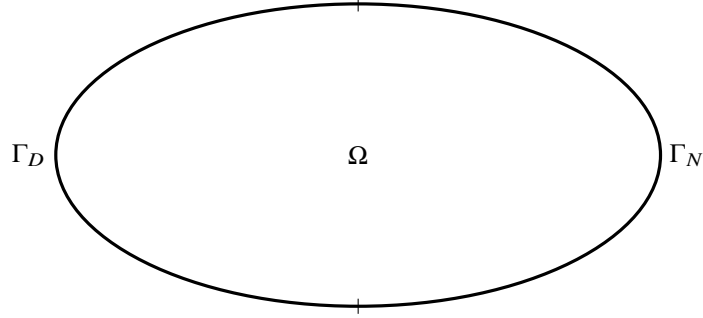


Figure 1: Physical domain

2.2 Domain Decomposition (DD) formulation

Let Ω_i , $i = 1, 2$ be open subsets of Ω , such that $\overline{\Omega} = \overline{\Omega_1 \cup \Omega_2}$, $\Omega_1 \cap \Omega_2 = \emptyset$. Denote $\Gamma_i := \partial\Omega_i \cap \Gamma$, $i = 1, 2$ and $\Gamma_0 := \overline{\Omega_1} \cap \overline{\Omega_2}$. In the same way we define the corresponding boundary subsets $\Gamma_{i,D}$ and $\Gamma_{i,N}$, $i = 1, 2$; see Figure 2.

Then the DD formulation reads as follows: for $i = 1, 2$, given $f_i : \Omega_i \rightarrow \mathbb{R}^2$ and $u_{i,D} : \Gamma_{i,D} \rightarrow \mathbb{R}^2$, find $u_i : \Omega_i \rightarrow \mathbb{R}^2$, $p_i : \Omega_i \rightarrow \mathbb{R}$ s.t.

$$-v\Delta u_i + (u_i \cdot \nabla) u_i + \nabla p_i = f_i \quad \text{in } \Omega_i, \quad (2a)$$

$$-\text{div} u_i = 0 \quad \text{in } \Omega_i, \quad (2b)$$

$$u_i = u_{i,D} \quad \text{on } \Gamma_{i,D}, \quad (2c)$$

$$v \frac{\partial u_i}{\partial n_i} - p_i n_i = 0 \quad \text{on } \Gamma_{i,N}, \quad (2d)$$

$$v \frac{\partial u_i}{\partial n_i} - p_i n_i = (-1)^{i+1} g \quad \text{on } \Gamma_0, \quad (2e)$$

for some $g : \Gamma_0 \rightarrow \mathbb{R}^2$.

Even though in the numerical simulations we will focus on the cases where $f_i = f|_{\Omega_i}$, $u_{i,D} = u_D|_{\Gamma_{i,D}}$ for $i = 1, 2$, the whole theoretical exposition in this paper works just as well for more general functions $f_1, f_2, u_{1,D}$ and $u_{2,D}$.

For any g the solution to the problem (2) is not the same as the solution to the problem (1), that is $u_1 \neq u|_{\Omega_1}$, $p_1 \neq p|_{\Omega_1}$, $u_2 \neq u|_{\Omega_2}$ and $p_2 \neq p|_{\Omega_2}$. On the other hand, there exists a choice for g , $g = \left(v \frac{\partial u_1}{\partial n_1} - p_1 n_1 \right) |_{\Gamma_0} = - \left(v \frac{\partial u_2}{\partial n_2} - p_2 n_2 \right) |_{\Gamma_0}$, such that the solutions to (2) coincide with the solution to (1) on the corresponding subdomains. Therefore, we must find such a g , so that u_1 is as close as possible to u_2 at the interface Γ_0 . One way to accomplish this is to minimise the functional

$$\mathcal{J}(u_1, u_2) =: \frac{1}{2} \int_{\Gamma_0} |u_1 - u_2|^2 d\Gamma. \quad (3)$$

Instead of (3) we can also consider the penalised or regularised functional

$$\mathcal{J}_\gamma(u_1, u_2; g) =: \frac{1}{2} \int_{\Gamma_0} |u_1 - u_2|^2 d\Gamma + \frac{\gamma}{2} \int_{\Gamma_0} |g|^2 d\Gamma, \quad (4)$$

where γ is a constant that can be chosen to change the relative importance of the terms in (4).

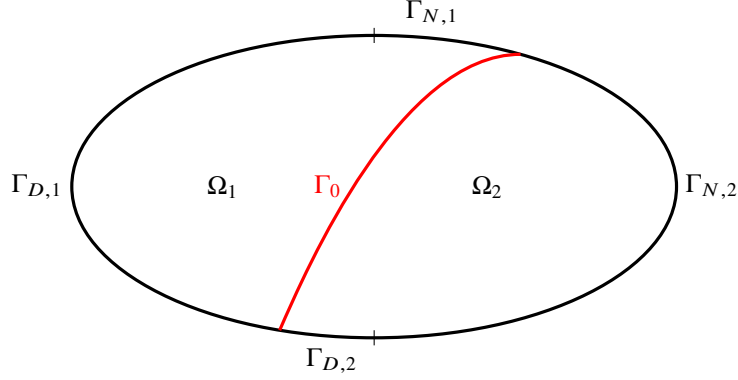


Figure 2: Domain Decomposition of the fluid domain

Thus we face an optimisation problem under PDE constraints: minimise the functional (3) (or (4)) over a suitable function g , subject to (2).

2.3 Variational Formulation of the PDE constraints

For $i = 1, 2$ define the following spaces:

- $V_i := \{u \in H^1(\Omega_i; \mathbb{R}^2)\}$,
- $V_{i,0} := \{u \in H^1(\Omega_i; \mathbb{R}^2) : u|_{\Gamma_{i,D}} = 0\}$,
- $Q_i := \{p \in L^2(\Omega_i; \mathbb{R})\}$.

The spaces V_i are endowed with the $H^1(\Omega_i)$ -norm for $i = 1, 2$, the spaces $V_{i,0}$ with the $H_0^1(\Omega_i)$ -norm and the spaces Q_i with the $L^2(\Omega_i)$ -norm for $i = 1, 2$.

Then, we define the following bilinear and trilinear forms: for $i=1,2$

- $a_i : V_i \times V_{i,0} \rightarrow \mathbb{R}, \quad a_i(u_i, v_i) = \nu(\nabla u_i, \nabla v_i)_{\Omega_i}$,
- $b_i : V_i \times Q_i \rightarrow \mathbb{R}, \quad b_i(v_i, q_i) = -(\operatorname{div} v_i, q_i)_{\Omega_i}$,
- $c_i : V_i \times V_i \times V_{i,0} \rightarrow \mathbb{R}, \quad c_i(u_i, w_i, v_i) = ((u_i \cdot \nabla) w_i, v_i)_{\Omega_i}$,

where $(\cdot, \cdot)_{\omega}$ indicates the $L^2(\omega)$ inner product.

Consequently, the variational counterpart of (2) reads as follows: for $i = 1, 2$, find $u_i \in V_i$ and $p_i \in Q_i$ s.t.

$$a_i(u_i, v_i) + c_i(u_i, u_i, v_i) + b_i(v_i, p_i) = (f_i, v_i)_{\Omega_i} + \left((-1)^{i+1} g, v_i \right)_{\Gamma_0} \quad \forall v_i \in V_{i,0}, \quad (5a)$$

$$b_i(u_i, q_i) = 0 \quad \forall q_i \in Q_i, \quad (5b)$$

$$u_i = u_{i,D} \quad \text{on } \Gamma_{i,D}. \quad (5c)$$

2.4 Optimality system

One of the ways to address the constrained optimisation problem is to reformulate the initial problem in terms of a Lagrangian functional by introducing the so-called adjoint variables. In

this way, the optimal solution to the original problem is sought among the stationary points of the Lagrangian, see, for instance, [19, 23].

We define the Lagrangian functional as follows:

$$\begin{aligned} \mathcal{L}(u_1, p_1, u_2, p_2, \xi_1, \xi_2, \lambda_1, \lambda_2; g) &:= \mathcal{J}_\gamma(u_1, u_2; g) \\ &\quad - \sum_{i=1}^2 [a_i(u_i, \xi_i) + c_i(u_i, u_i, \xi_i) \\ &\quad + b_i(\xi_i, p_i) + b_i(u_i, \lambda_i)] \\ &\quad + \sum_{i=1}^2 (f_i, \xi_i)_{\Omega_i} + \sum_{i=1}^2 ((-1)^{i+1} g, \xi_i)_{\Gamma_0}. \end{aligned} \quad (6)$$

Notice that technically we should have also included Lagrange multipliers corresponding to the non-homogeneous Dirichlet boundary conditions (5c) in the definition of the functional \mathcal{L} , but since the functional \mathcal{J}_γ does not explicitly depend on $u_{1,D}$ and $u_{2,D}$ the corresponding Dirichlet boundary conditions for the adjoint equation that we are going to derive below will be homogeneous on these parts of the boundaries.

We now apply the necessary conditions for finding stationary points of \mathcal{L} . Setting to zero the first variations w.r.t. ξ_i and λ_i , $i = 1, 2$ yields the state equations (5a)-(5b). Setting to zero the first variations w.r.t. u_1 , p_1 , u_2 and p_2 yields the adjoint equations:

$$\begin{aligned} a_i(\eta_i, \xi_i) + c_i(\eta_i, u_i, \xi_i) + c_i(u_i, \eta_i, \xi_i) + b_i(\eta_i, \lambda_i) \\ = ((-1)^{i+1} \eta_i, u_1 - u_2)_{\Gamma_0}, \quad \forall \eta_i \in V_{i,0}, \end{aligned} \quad (7a)$$

$$b_i(\xi_i, \mu_i) = 0, \quad \forall \mu_i \in Q_i. \quad (7b)$$

Finally, setting to zero the first variations w.r.t. g yields the optimality condition:

$$\gamma(h, g)_{\Gamma_0} + (h, \xi_1 - \xi_2)_{\Gamma_0} = 0, \quad \forall h \in L^2(\Gamma_0). \quad (8)$$

2.5 Sensitivity derivatives

In order to obtain the expression for the gradient of the optimisation problem in hand, we will resort to the sensitivity approach, see, for instance, [19, 23]. The approach consists of finding equations for direction derivatives of the state variable with respect to control, called sensitivities.

The first derivative $\frac{d\mathcal{J}_\gamma}{dg}$ of \mathcal{J}_γ is defined through its action on variation \tilde{g} as follows:

$$\left\langle \frac{d\mathcal{J}_\gamma}{dg}, \tilde{g} \right\rangle = (u_1 - u_2, \tilde{u}_1 - \tilde{u}_2)_{\Gamma_0} + \gamma(g, \tilde{g})_{\Gamma_0}, \quad (9)$$

where $\tilde{u}_1 \in V_{1,0}$, $\tilde{u}_2 \in V_{2,0}$ are the solutions to:

$$\begin{aligned} a_i(\tilde{u}_i, v_i) + c_i(\tilde{u}_i, u_i, v_i) + c_i(u_i, \tilde{u}_i, v_i) \\ + b_i(v_i, \tilde{p}_i) = ((-1)^{i+1} \tilde{g}, v_i)_{\Gamma_0} \quad \forall v_i \in V_{i,0}, \end{aligned} \quad (10a)$$

$$b_i(\tilde{u}_i, q_i) = 0 \quad \forall q_i \in Q_i. \quad (10b)$$

We can make use of the adjoint equations (7) in order to find the representation of the gradient of the functional \mathcal{J}_γ . Let ξ_1 and ξ_2 be the solutions to (7), \tilde{u}_1 and \tilde{u}_2 be the solutions to (10). By setting $\eta_i = \tilde{u}_i$ in (7a), $\mu_i = \tilde{p}_i$ in (7b), $v_i = \xi_i$ in (10a) and $q_i = \lambda_i$ in (10b) we obtain:

$$(u_1 - u_2, \tilde{u}_1 - \tilde{u}_2)_{\Gamma_0} = (\tilde{g}, \xi_1 - \xi_2)_{\Gamma_0},$$

so that it yields the explicit formula for the gradient of \mathcal{J}_γ :

$$\frac{d\mathcal{J}_\gamma}{dg}(u_1, u_2; g) = \gamma g + (\xi_1 - \xi_2)|_{\Gamma_0}, \quad (11)$$

where ξ_1 and ξ_2 are determined from g through (7). Notice that the gradient expression (11) is consistent with the optimality condition (8) derived in the previous section.

3 Gradient-based algorithm for PDE-constraint optimisation problem

In view of being able to provide a closed-form formula for the gradient for the objective functional \mathcal{J}_γ , the natural way to proceed is to resort to a gradient-based iterative optimisation algorithm.

In order to keep the exposition simple, we will describe the idea using the steepest decent method. We consider the following simple gradient method: given a starting guess $g^{(0)}$, let

$$g^{(n+1)} = g^{(n)} - \alpha \frac{d\mathcal{J}_\gamma}{dg}(u_1^{(n)}, u_2^{(n)}; g^{(n)}). \quad (12)$$

Combining this with (11) we obtain:

$$g^{(n+1)} = g^{(n)} - \alpha (\gamma g^{(n)} + (\xi_1^{(n)} - \xi_2^{(n)})|_{\Gamma_0}), \quad (13)$$

or

$$g^{(n+1)} = (1 - \alpha\gamma) g^{(n)} - \alpha (\xi_1^{(n)} - \xi_2^{(n)})|_{\Gamma_0}, \quad (14)$$

where $\xi_1^{(n)}$ and $\xi_2^{(n)}$ are determined from (7) with g replaced by $g^{(n)}$.

In summary, we have the following algorithm:

Algorithm 1.

1. Choose $g^{(0)}$, α .
2. For $n=0,1,2,\dots$ until convergence
 - (a) Determine $u_1^{(n)} \in V_1, u_2^{(n)} \in V_2$ by solving (5a)–(5b) with $g = g^{(n)}$.
 - (b) Determine $\xi_1^{(n)} \in V_{1,0}, \xi_2^{(n)} \in V_{2,0}$ by solving (7) with $u_1 = u_1^{(n)}, u_2 = u_2^{(n)}$.
 - (c) Update $g^{(n+1)}$ by setting

$$g^{(n+1)} := (1 - \alpha\gamma) g^{(n)} - \alpha (\xi_1^{(n)} - \xi_2^{(n)})|_{\Gamma_0}.$$

In practice, the typical methods used to solve problems like the one considered in this paper are Broyden–Fletcher–Goldfarb–Shanno (BFGS) and Newton Conjugate Gradient (CG) algorithms which tend to show much faster convergence and higher efficiency with respect to the steepest-decent algorithm.

4 Finite Element Discretisation

In this section, we present the Finite Element spatial discretisation for the optimal control problem previously introduced. We assume to have at hand two well-defined triangulations \mathcal{T}_1 and \mathcal{T}_2 over the domains Ω_1 and Ω_2 respectively, and an extra lower-dimensional triangulation \mathcal{T}_0 of the

interface Γ_0 ; additionally, we assume that \mathcal{T}_1 , \mathcal{T}_2 and \mathcal{T}_0 share the same degrees of freedom relative to the interface Γ_0 . We can then define usual Lagrangian FE spaces $V_{i,h} \subset V_i$, $V_{i,0,h} \subset V_{i,0}$, $Q_{i,h} \subset Q_i$, $i = 1, 2$ and $X_h \subset L^2(\Gamma_0)$ endowed with $L^2(\Gamma_0)$ -norm. Since the problems at hand have a saddle-point structure, in order to guarantee the well-posedness of the discretised problem, we require the FE spaces to satisfy the following inf-sup conditions: there exist positive constants c_1, c_2, c_3 and c_4 s.t.

$$\inf_{q_{i,h} \in Q_{i,h} \setminus \{0\}} \sup_{v_{i,h} \in V_{i,h} \setminus \{0\}} \frac{b_i(v_{i,h}, q_{i,h})}{\|v_{i,h}\|_{V_{i,h}} \|q_{i,h}\|_{Q_{i,h}}} \geq c_i, \quad i = 1, 2, \quad (15)$$

$$\inf_{q_{i,h} \in Q_{i,h} \setminus \{0\}} \sup_{v_{i,h} \in V_{i,0,h} \setminus \{0\}} \frac{b_i(v_{i,h}, q_{i,h})}{\|v_{i,h}\|_{V_{i,0,h}} \|q_{i,h}\|_{Q_{i,h}}} \geq c_{i+2}, \quad i = 1, 2. \quad (16)$$

A very common choice in this framework is to use the so-called Taylor–Hood finite element spaces, namely the Lagrange polynomial approximation of the second-order for velocity and of the first-order for pressure. We point out that the order of the polynomial space X_h will not lead to big computational efforts as it is defined on the 1-dimensional curve Γ_0 .

Using the Galerkin projection we can derive the following discretised optimisation problem: minimise over $g_h \in X_h$ the functional:

$$\mathcal{J}_{\gamma,h}(u_{1,h}, u_{2,h}; g_h) := \frac{1}{2} \int_{\Gamma_0} |u_{1,h} - u_{2,h}|^2 d\Gamma + \frac{\gamma}{2} \int_{\Gamma_0} |g_h|^2 d\Gamma \quad (17)$$

under the constraints that $u_{i,h} \in V_{i,h}$, $p_{i,h} \in Q_{i,h}$ satisfy the following variational equations for $i = 1, 2$:

$$a_i(u_{i,h}, v_{i,h}) + c_i(u_{i,h}, u_{i,h}, v_{i,h}) + b_i(v_{i,h}, p_{i,h}) \quad \forall v_{i,h} \in V_{i,0,h}, \quad (18a)$$

$$= (f_i, v_{i,h})_{\Omega_i} + ((-1)^{i+1} g_h, v_{i,h})_{\Gamma_0} \quad \forall q_{i,h} \in Q_{i,h}, \quad (18b)$$

$$b_i(u_{i,h}, q_{i,h}) = 0 \quad \text{on } \Gamma_{i,D}, \quad (18c)$$

$$u_{i,h} = u_{i,D,h}$$

where $u_{i,D,h}$ is the Galerkin projection of $u_{i,D}$ onto the trace-space $V_{i,h}|_{\Gamma_{i,D}}$.

Notice that the structure of the equations (18) and of the functional (17) is the same as the one of the continuous case so that it enables us to provide the following expression of the gradient of the discretised functional (17):

$$\frac{d\mathcal{J}_{\gamma,h}}{dg_h}(u_{1,h}, u_{2,h}; g_h) = \gamma g_h + (\xi_{1,h} - \xi_{2,h})|_{\Gamma_0}, \quad (19)$$

where $\xi_{1,h}$ and $\xi_{2,h}$ are the solutions to the discretised adjoint problem: for $i = 1, 2$ find $\xi_{i,h} \in V_{i,0,h}$ and $\lambda_{i,h} \in Q_{i,h}$ that satisfy

$$a_i(\eta_{i,h}, \xi_{i,h}) + c_i(\eta_{i,h}, u_{i,h}, \xi_{i,h}) + c_i(u_{i,h}, \eta_{i,h}, \xi_{i,h}) \quad \forall \eta_{i,h} \in V_{i,0,h}, \quad (20a)$$

$$+ b_i(\eta_{i,h}, \lambda_{i,h}) = ((-1)^{i+1} \eta_{i,h}, u_{1,h} - u_{2,h})_{\Gamma_0}, \quad \forall \mu_{i,h} \in Q_{i,h}. \quad (20b)$$

$$b_i(\xi_{i,h}, \mu_{i,h}) = 0,$$

We would also like to stress that at the algebraic level the discretised minimisation problem can be recast in the setting of the finite-dimensional space \mathbb{R}^p , where p is the number of Finite Element degrees of freedom which belong to the interface Γ_0 .

5 Reduced-Order Model

As it was highlighted in section 1, Reduced-Order methods are efficient tools for significant reduction of the parameter-dependent PDEs. This section deals with the reduced-order model for the problem obtained in the previous section, where the state equations, namely Navier-Stokes equations, are assumed to be dependent on a set of physical parameters. First, we introduce two practical ingredients we will be using in the course of the reduced-basis generation, namely a lifting function and the pressure supremiser enrichment. Then, we describe the offline phase based on the Proper Orthogonal Decomposition technique, which is followed by the online phase based on a Galerkin projection onto the reduced spaces.

5.1 Lifting Function and Velocity Supremiser Enrichment

In the following, we are going to discuss a snapshot compression technique for the generation of reduced basis functions. In order to do so we need to introduce two important ingredients in this context, namely the lifting function technique and the supremiser enrichment of the velocity space.

The use of lifting functions is quite common in the reduced basis method (RBM) framework; see, for example, [22, 5]. It is motivated by the fact that in the chosen model we are supposed to tackle the non-homogeneous Dirichlet boundary condition on the parts of the boundaries $\Gamma_{i,D}$, $i = 1, 2$. From the implementation point of view, this does not present any problem when dealing with the high-fidelity model since there are several well-known techniques for non-homogeneous essential conditions, in particular at the algebraic level. However, these boundary conditions create some problems when dealing with the reduced basis methods. Indeed, we seek to generate a linear vector space which is obtained by the compression of the set of snapshots, and this clearly cannot be achieved by using snapshots which satisfy different Dirichlet conditions – the resulting space would not be linear. This problem is solved by introducing a lifting function $l_{i,h} \in V_{i,h}$, $i = 1, 2$ during the offline stage, such that $l_{i,h} = u_{i,D,h}$ on $\Gamma_{i,D}$. We define two new variables $u_{i,0,h} \in V_{i,0,h}$, $i = 1, 2$ by setting $u_{i,0,h} := u_{i,h} - l_{i,h}$. Clearly, the variables $u_{i,0,h}$, $i = 1, 2$ satisfy the homogeneous condition $u_{i,0,h} = 0$ on $\Gamma_{i,D}$ and so they can be used to generate the reduced basis linear space. We remark that the lifting function is needed only in the domain where the Dirichlet boundary is non-empty, i.e. where $\Gamma_{i,D} \neq \emptyset$ for $i = 1, 2$. It is important to point out that the choice of lifting functions is not unique; in our work, we chose to use the solution of the Stokes problem in one of the domains Ω , Ω_1 or Ω_2 (depending on the particular model we are investigating) with the velocity equal to u_D on the corresponding parts of the boundaries and the homogeneous Neumann conditions analogous to the original problem setting.

The other ingredient we will use in the following exposition is the so-called velocity supremiser. This is necessary to obtain a stable approximation of the saddle-point problem at the reduced level discussed in the following subsections. The well-posedness of the problem is again assured by satisfying the inf-sup conditions like (16). The supremiser variables $s_{i,h}$, $i = 1, 2$ are defined as the solution to the following problem: find $s_{i,h} \in V_{i,0,h}$ such that

$$(\nabla v_{i,h}, \nabla s_{i,h}) = b_{i,h}(v_{i,h}, p_{i,h}) \quad \forall v_{i,h} \in V_{i,0,h}, \quad (21)$$

where $p_{i,h}$, $i = 1, 2$ are the finite-element pressure solutions of the Navier-Stokes problem and the left-hand side is the scalar product which defines a norm on the space $V_{i,0,h}$. For more details, we refer to [5, 15].

5.2 Reduced Basis Generation

Once we obtain the homogenised snapshots $u_{i,0,h}$ and the pressure supremisers $s_{i,h}$ for $i = 1, 2$, we are ready to construct a set of reduced basis functions. A very common choice when dealing with Navier-Stokes equations is to use the Proper Orthogonal Decomposition (POD) technique, which is based on the Singular Value Decomposition of the snapshot matrices; see, for instance, [22]. In order to implement this technique we will need two main ingredients: the matrices of the inner products and the snapshot matrices. First, we define the basis functions for the FE element spaces used in the weak formulation (17), (18) and (20) as follows:

$$\begin{aligned}\mathcal{U}_{i,0,h} &= \left\{ \phi_1^{u_i}, \dots, \phi_{\mathcal{N}_h^{u_i}}^{u_i} \right\} - \text{the FE basis of the space } V_{i,0,h}, i = 1, 2, \\ \mathcal{P}_{i,h} &= \left\{ \phi_1^{p_i}, \dots, \phi_{\mathcal{N}_h^{p_i}}^{p_i} \right\} - \text{the FE basis of the space } Q_{i,h}, i = 1, 2, \\ \Xi_{i,0,h} &= \left\{ \phi_1^{\xi_i}, \dots, \phi_{\mathcal{N}_h^{\xi_i}}^{\xi_i} \right\} - \text{the FE basis of the space } V_{i,0,h}, i = 1, 2, \\ \mathcal{G}_{i,h} &= \left\{ \phi_1^g, \dots, \phi_{\mathcal{N}_h^g}^g \right\} - \text{the FE basis of the space } X_h,\end{aligned}$$

where $\mathcal{N}_h^*, * \in \{u_1, p_1, u_2, p_2, \xi_1, \xi_2, g\}$ denotes the dimension of the corresponding FE space. We notice that, in principle, the bases $\mathcal{U}_{i,0,h}$ and $\Xi_{i,0,h}$ may not contain the same functions though they have the same cardinality, i.e. $\mathcal{N}_h^{u_i} = \mathcal{N}_h^{\xi_i}$; this is the case if we choose different Finite Element spaces for the approximation of the state and adjoint velocities.

We proceed by building the snapshot matrices. In doing so we sample a parameter space and draw a discrete set of M parameter values; there are various sampling techniques, among which we point out the uniform sampling. Then, the snapshots are taken as a high-fidelity, i.e. Finite Element, solutions at each parameter value in the sampling set.

We proceed by building the snapshot matrices $\mathcal{S}_{u_i} \in \mathbb{R}^{\mathcal{N}_h^{u_i} \times 4M}$, $\mathcal{S}_{s_i} \in \mathbb{R}^{\mathcal{N}_h^{s_i} \times 4M}$, $\mathcal{S}_{p_i} \in \mathbb{R}^{\mathcal{N}_h^{p_i} \times 4M}$, $\mathcal{S}_{\xi_i} \in \mathbb{R}^{\mathcal{N}_h^{\xi_i} \times 2M}$ for $i = 1, 2$ and $\mathcal{S}_g \in \mathbb{R}^{\mathcal{N}_h^g \times M}$ defined as follows:

$$\begin{aligned}\mathcal{S}_{u_1} &= [u_{1,0,h}^1, \dots, u_{1,0,h}^M, 0, \dots, 0, 0, \dots, 0, 0, \dots, 0], \\ \mathcal{S}_{s_1} &= [s_{1,h}^1, \dots, s_{1,h}^M, 0, \dots, 0, 0, \dots, 0, 0, \dots, 0], \\ \mathcal{S}_{p_1} &= [0, \dots, 0, p_{1,h}^1, \dots, p_{1,h}^M, 0, \dots, 0, 0, \dots, 0], \\ \mathcal{S}_{u_2} &= [0, \dots, 0, 0, \dots, 0, u_{2,0,h}^1, \dots, u_{2,0,h}^M, 0, \dots, 0], \\ \mathcal{S}_{s_2} &= [0, \dots, 0, 0, \dots, 0, s_{2,h}^1, \dots, s_{2,h}^M, 0, \dots, 0], \\ \mathcal{S}_{p_2} &= [0, \dots, 0, 0, \dots, 0, 0, \dots, 0, p_{2,h}^1, \dots, p_{2,h}^M], \\ \mathcal{S}_{\xi_1} &= [\xi_{1,h}^1, \dots, \xi_{1,h}^M, 0, \dots, 0], \quad \mathcal{S}_{\xi_2} = [0, \dots, 0, \xi_{2,h}^1, \dots, \xi_{2,h}^M], \\ \mathcal{S}_g &= [g_h^1, \dots, g_h^M],\end{aligned}$$

where $\mathcal{N}_h^s = \mathcal{N}_h^{u_1} + \mathcal{N}_h^{p_1} + \mathcal{N}_h^{u_2} + \mathcal{N}_h^{p_2}$, $\mathcal{N}_h^a = \mathcal{N}_h^{\xi_1} + \mathcal{N}_h^{\xi_2}$ and M is the number of snapshots.

Notice that since all the snapshots of the variables $\xi_{1,h}$ and $\xi_{2,h}$ are divergence-free on the domain of definition, the reduced spaces constructed for those variables will already contain this information, so that it allows us not to store the snapshots of the variables $\lambda_{1,h}$ and $\lambda_{2,h}$, which are playing the role of the Lagrange multipliers relative to the divergence free-conditions, as they do not contain any important information.

The next step is to define the inner-product matrices X_{u_i} , X_{p_i} , X_{ξ_i} for $i = 1, 2$ and X_g . These matrices have the block diagonal structure as follows:

$$\begin{aligned}
X_{u_1} &= \text{diag}(x_{u_1}, 0_{p_1}, 0_{u_2}, 0_{p_2}), \\
X_{p_1} &= \text{diag}(0_{u_1}, x_{p_1}, 0_{u_2}, 0_{p_2}), \\
X_{u_2} &= \text{diag}(0_{u_1}, 0_{p_1}, x_{u_2}, 0_{p_2}), \\
X_{p_2} &= \text{diag}(0_{u_1}, 0_{p_1}, 0_{u_2}, x_{p_2}), \\
X_{\xi_1} &= \text{diag}(x_{\xi_1}, 0_{\xi_2}), \\
X_{\xi_2} &= \text{diag}(0_{\xi_1}, x_{\xi_2}), \\
X_g &= x_g.
\end{aligned}$$

Above, we used the following notations: $0_* \in \mathbb{R}^{N_h^* \times N_h^*}$ is a zero square matrix of dimension $N_h^* \times N_h^*$, where $*$ $\in \{u_1, p_1, u_2, p_2, \xi_1, \xi_2, g\}$ and

$$\begin{aligned}
(x_{u_i})_{jk} &= \left(\nabla \phi_k^{u_i}, \nabla \phi_j^{u_i} \right)_{\Omega_i}, \quad \text{for } j, k = 1, \dots, N_h^{u_i}, \quad i = 1, 2, \\
(x_{p_i})_{jk} &= \left(\phi_k^{p_i}, \phi_j^{p_i} \right)_{\Omega_i}, \quad \text{for } j, k = 1, \dots, N_h^{p_i}, \quad i = 1, 2, \\
(x_{\xi_i})_{jk} &= \left(\nabla \phi_k^{\xi_i}, \nabla \phi_j^{\xi_i} \right)_{\Omega_i}, \quad \text{for } j, k = 1, \dots, N_h^{\xi_i}, \quad i = 1, 2, \\
(x_g)_{jk} &= \left(\phi_k^g, \phi_j^g \right)_{\Gamma_0}, \quad \text{for } j, k = 1, \dots, N_h^g.
\end{aligned}$$

We are now ready to introduce the correlation matrices C_{u_i} , C_{s_i} , C_{p_i} , C_{ξ_i} for $i = 1, 2$ and C_g , all of dimension $M \times M$, as:

$$C_* := S_*^T X_* S_*$$

for every $*$ $\in \{u_1, p_1, u_2, p_2, \xi_1, \xi_2, g\}$ and

$$C_{s_i} := S_{s_i}^T X_{u_i} S_{s_i}, \quad i = 1, 2.$$

Once we have built the correlation matrices, we are able to carry out a POD compression on the sets of snapshots. This can be achieved by solving the following eigenvalue problems:

$$C_* Q_* = Q_* \Lambda_* \tag{22}$$

where $*$ $\in \{u_1, s_1, p_1, u_2, s_2, p_2, \xi_1, \xi_2, g\}$, Q_* is the eigenvectors matrix and Λ_* is the diagonal eigenvalues matrix with eigenvalues ordered by decreasing order of their magnitude. The k -th reduced basis function for the component $*$ is then obtained by applying the matrix S_* to v_k^* – the k -th column vector of the matrix Q_* :

$$\Phi_k^* := \frac{1}{\sqrt{\lambda_k^*}} S_* v_k^*,$$

where λ_k^* is the k -th eigenvalue from (22). Therefore, we are able to form the set of reduced basis as

$$\begin{aligned}
\mathcal{A}^s &:= \bigcup_{* \in \{u_1, s_1, p_1, u_2, s_2, p_2\}} \left\{ \Psi_1^*, \dots, \Psi_{N_*}^* \right\}, \\
\mathcal{A}^a &:= \bigcup_{* \in \{\xi_1, \xi_2\}} \left\{ \Psi_1^*, \dots, \Psi_{N_*}^* \right\},
\end{aligned}$$

$$\mathcal{A}^g := \left\{ \Phi_1^g, \dots, \Phi_{N_g}^g \right\},$$

where the integer numbers N_* indicate the number of the basis functions used for each component and

$$\begin{aligned} \Psi_k^{u_1} &= \begin{pmatrix} \Phi_k^{u_1} \\ 0 \\ 0 \\ 0 \end{pmatrix}, \quad \Psi_k^{s_1} = \begin{pmatrix} \Phi_k^{s_1} \\ 0 \\ 0 \\ 0 \end{pmatrix}, \quad \Psi_k^{p_1} = \begin{pmatrix} 0 \\ \Phi_k^{p_1} \\ 0 \\ 0 \end{pmatrix}, \quad \Psi_k^{u_2} = \begin{pmatrix} 0 \\ 0 \\ \Phi_k^{u_2} \\ 0 \end{pmatrix}, \\ \Psi_k^{s_2} &= \begin{pmatrix} 0 \\ 0 \\ \Phi_k^{s_2} \\ 0 \end{pmatrix}, \quad \Psi_k^{p_2} = \begin{pmatrix} 0 \\ 0 \\ 0 \\ \Phi_k^{p_2} \end{pmatrix}, \quad \Psi_k^{\xi_1} = \begin{pmatrix} \Phi_k^{\xi_1} \\ 0 \end{pmatrix}, \quad \Psi_k^{\xi_2} = \begin{pmatrix} 0 \\ \Phi_k^{\xi_2} \end{pmatrix}. \end{aligned}$$

We note that the first and the third blocks include both the u_1 , s_1 and the u_2 , s_2 basis functions - it is here that we use the pressure supremiser enrichment of the velocities spaces discussed at the beginning of this section. We provide the following renumbering of the functions for further simplicity:

$$\Phi_{N_{u_i}+k}^{u_i} := \Phi_k^{s_i}, \quad \Psi_{N_{u_i}+k}^{u_i} := \Psi_k^{s_i}, \quad \text{for } k = 1, \dots, N_{s_i}, \quad i = 1, 2,$$

and we redefine $N_{u_i} := N_{u_i} + N_{s_i}$, $i = 1, 2$.

Finally, we introduce three separate reduced basis spaces - for the state, the adjoint and the control variables, respectively:

$$\begin{aligned} V_N^s &= \text{span} \mathcal{A}^s, & \dim V_N^s &= N_{u_1} + N_{p_1} + N_{u_2} + N_{p_2}, \\ V_N^a &= \text{span} \mathcal{A}^a, & \dim V_N^a &= N_{\xi_1} + N_{\xi_2}, \\ V_N^g &= \text{span} \mathcal{A}^g, & \dim V_N^g &= N_g. \end{aligned}$$

5.3 Online Phase

Once we have introduced the reduced basis spaces we can define the reduced function expansions

$$U_N = (u_{1,0,N}, p_{1,N}, u_{2,0,N}, p_{2,N}) \in V_N^s, \quad \Xi_N = (\xi_{1,N}, \xi_{2,N}) \in V_N^a, \quad g_N \in V_N^g$$

as

$$\begin{aligned} u_{i,0,N} &:= \sum_{k=1}^{N_{u_i}} \underline{u}_{i,0,k} \Phi_k^{u_i}, \quad i = 1, 2, & \xi_{i,N} &:= \sum_{k=1}^{N_{\xi_i}} \underline{\xi}_{i,k} \Phi_k^{\xi_i}, \quad i = 1, 2, \\ p_{i,N} &:= \sum_{k=1}^{N_{p_i}} \underline{p}_{i,k} \Phi_k^{p_i}, \quad i = 1, 2, & g_N &:= \sum_{k=1}^{N_g} \underline{g}_k \Phi_k^g. \end{aligned}$$

In the previous equations, the underscore indicates the coefficients of the basis expansion of the reduced solution. Then the online reduced problem reads as follows: minimise over $g_N \in V_N^g$ the functional

$$\mathcal{J}_{\mathcal{Y},N}(u_{1,N}, u_{2,N}; g_N) := \frac{1}{2} \int_{\Gamma_0} |u_{1,N} - u_{2,N}|^2 d\Gamma + \frac{\gamma}{2} \int_{\Gamma_0} |g_N|^2 d\Gamma \quad (23)$$

where $u_{1,N} = u_{1,0,N} + l_{1,N}$, $u_{2,N} = u_{2,0,N} + l_{2,N}$ for $(u_{1,0,N}, p_{1,N}, u_{2,0,N}, p_{2,N}) \in V_N^S$ satisfy the following reduced equations for every $v_N = (v_{1,N}, q_{1,N}, v_{2,N}, q_{2,N}) \in V_N^S$:

$$\begin{aligned} a_i(u_{i,0,N}, v_{i,N}) &+ c_i(u_{i,0,N}, u_{i,0,N}, v_{i,N}) + c_i(u_{i,0,N}, l_{i,N}, v_{i,N}) \\ &+ c_i(l_{i,N}, u_{i,0,N}, v_{i,N}) + b_i(v_{i,N}, p_{i,N}) \\ &= (f_i, v_{i,N})_{\Omega_i} + ((-1)^{i+1} g_N, v_{i,N})_{\Gamma_0} \\ &\quad - a_i(l_{i,N}, v_{i,N}) - c_i(l_{i,N}, l_{i,N}, v_{i,N}) \end{aligned} \quad (24a)$$

$$b_i(u_{i,0,N}, q_{i,N}) = -b_i(l_{i,N}, q_{i,N}), \quad (24b)$$

where $l_{i,N}$ is the Galerkin projection of the lifting function $l_{i,h}$ to the finite dimensional vector space spanned by the i -th velocity basis functions and $i = 1, 2$.

Similarly to the offline phase, we notice that the structure of the equations (24) and the functional (23) are the same as the ones of the continuous case, so this enables us to provide the following expression of the gradient of the reduced functional (23):

$$\frac{d\mathcal{J}_{\gamma,N}}{dg_N}(u_{1,N}, u_{2,N}; g_N) = \gamma g_N + (\xi_{1,N} - \xi_{2,N})|_{\Gamma_0}, \quad (25)$$

where $(\xi_{1,N}, \xi_{2,N}) \in V_N^a$ are the solutions to the reduced adjoint problem: find $(\xi_{1,N}, \xi_{2,N}) \in V_N^a$ such that it satisfies, for each pair of test functions $(\eta_{1,N}, \eta_{2,N}) \in V_N^a$ and $i = 1, 2$,

$$\begin{aligned} a_i(\eta_{i,N}, \xi_{i,N}) + c_i(\eta_{i,N}, u_{i,N}, \xi_{i,N}) + c_i(u_{i,N}, \eta_{i,N}, \xi_{i,N}) \\ = ((-1)^{i+1} \eta_{i,N}, u_{1,N} - u_{2,N})_{\Gamma_0}. \end{aligned} \quad (26)$$

Notice that the reduced adjoint equations no longer contain any terms corresponding to the bilinear forms $b_i(\cdot, \cdot)$, $i = 1, 2$. Indeed, as was previously mentioned, all the functions belonging to the reduced space V_N^a are already divergence-free by construction, so the aforementioned terms are automatically satisfied.

We would also like to stress that from the numerical implementation point of view the reduced minimisation problem can be recast in the setting of the finite-dimensional space \mathbb{R}^p , where p is the number of reduced basis function used for the control variable g_N in the online phase, that is $p = N_g$.

6 Numerical Results

We now present some numerical results obtained by applying the two-domain decomposition optimisation algorithm to the backward-facing step and the lid-driven cavity flow benchmarks.

All the numerical simulations for the offline phase were obtained using the software multiphenics [1], whereas the online phase simulations were carried out using RBniCS [2].

6.1 Backward-facing step test case

We start with introducing the backward-facing step flow test case. Figure 3 represents the physical domain of interest. The upper part of the channel has a length of 18 cm, the lower part 14 cm; the height of the left chamber is 3 cm, and the height of the right one is 5 cm. The splitting into two domains is performed by dissecting the domain by a vertical segment at the distance $\frac{26}{3}$ cm from the beginning of the channel as shown in Figure 4.

We impose homogeneous Dirichlet boundary conditions on the top and the bottom walls of the boundary Γ_{wall} for the fluid velocity, and homogeneous Neumann conditions on the outlet Γ_{out} , meaning that we assume free outflow on this portion of the boundary.

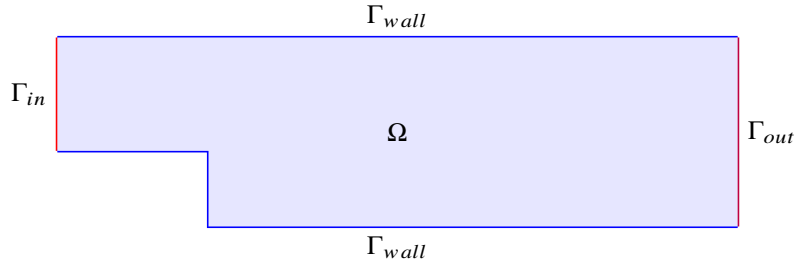


Figure 3: Physical domain for the backward-facing step problem

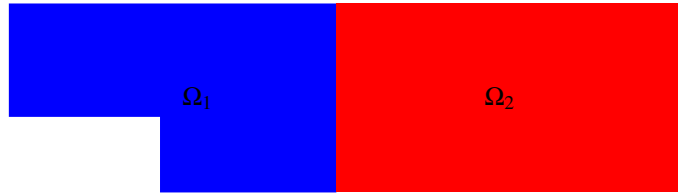
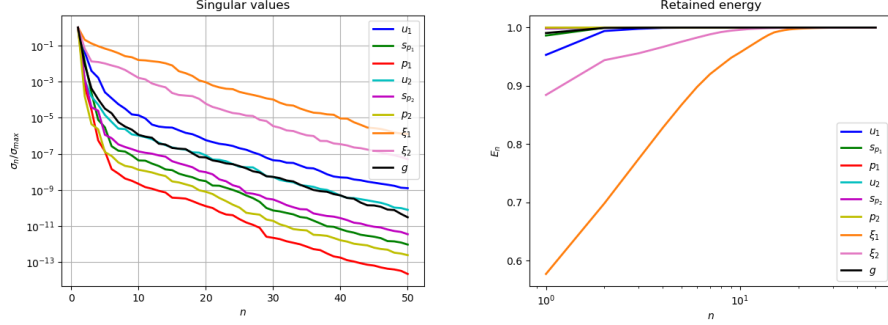


Figure 4: Domain decomposition for the backward-facing step problem domain

Physical parameters	2 : ν, \bar{U}
Range ν	[0.5, 2]
Range \bar{U}	[0.5, 6.5]
FE velocity order	2
FE pressure order	1
Total number of FE dofs	27,890
Number of FE dofs at the interface	130
Optimisation algorithm	L-BFGS-B
It_{max}	40
Tol_{opt}	10^{-5}
M	900
N_{max}	50

Table 1: Computational details of the offline stage.



(a) POD singular values as a function of number n of POD modes (log scaling in y -direction) (b) Energy retained by the first N_{max} POD modes (log scaling in x -direction)

Figure 5: Results of the offline stage: POD singular eigenvalue decay (a) and retained energy (b) of the first N_{max} POD modes

We impose a parabolic profile u_{in} on the inlet boundary Γ_{in} , where

$$u_{in}(x, y) = \begin{pmatrix} w(y) \\ 0 \end{pmatrix} \quad (27)$$

with $w(y) = \bar{U} \times \frac{4}{9}(y-2)(5-y)$, $y \in [2, 5]$; values of \bar{U} are reported in Table 1. Two physical parameters are considered: the viscosity ν and the maximal magnitude \bar{U} of the inlet velocity profile u_{in} . Details of the offline stage and the finite-element discretisation are summarised in Table 1. High-fidelity solutions are obtained by carrying out the minimisation in the space of dimension equal to the number of degrees of freedom at the interface, which is 130 in our test case. The best performance has been achieved by using the limited-memory Broyden–Fletcher–Goldfarb–Shanno (L-BFGS-B) optimisation algorithm, and two stopping criteria were applied: either the maximal number of iteration It_{max} is reached or the gradient norm of the target functional is less than the given tolerance Tol_{opt} .

Snapshots are sampled from a training set of M parameters uniformly sampled in the 2-dimensional parameter space, and the first N_{max} POD modes have been retained. Figure 5a shows the POD singular values for all the state, the adjoint and the control variables. As it can be seen, the POD singular values corresponding to the adjoint velocities ξ_1 and ξ_2 feature a slower decay compared to the one for the other variables. In Figure 5b, we can see the behaviour of the energy E_n retained by the first N modes for different components of the solution. Here, the retained energy for the component $* \in \{u_1, s_1, p_1, u_2, s_2, p_2, \xi_1, \xi_2, g\}$ is defined as:

$$E_n^* := \frac{\sum_{k=1}^n |\lambda_k^*|}{\sum_{k=1}^{N^*} |\lambda_k^*|}.$$

As we can see from the definition, the retained energy gives us an idea on the number of modes we would need to choose to preserve all the necessary physical information in the reduced model. In particular, we can see that the highest number of modes is needed to correctly represent the adjoint variables ξ_1 and ξ_2 .

Figures 6–9 represent the first four POD modes for each of the variables $u_1, u_2, s_1, s_2, p_1, p_2, \xi_1$ and ξ_2 . We stress that the POD modes were obtained separately for each component

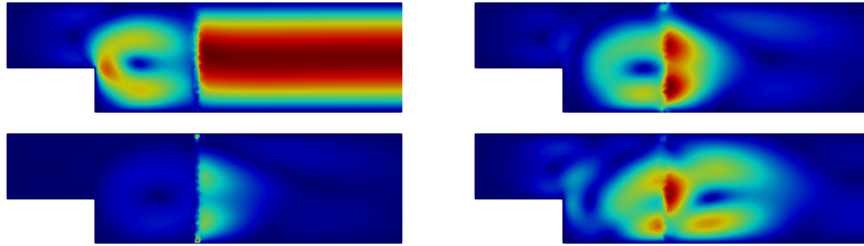


Figure 6: The first POD modes for the velocities u_1 and u_2 (subdomain functions are glued together for visualisation purposes).

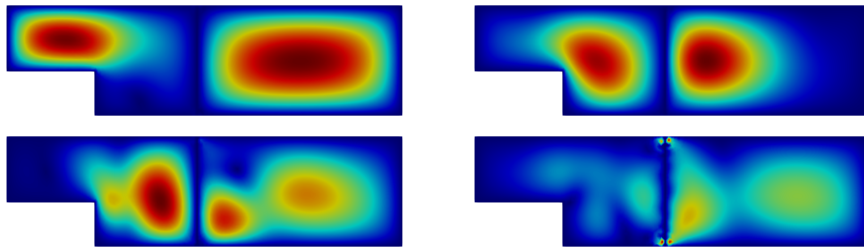


Figure 7: The first POD modes for the pressure supremisers s_1 and s_2 (subdomain functions are glued together for visualisation purposes).

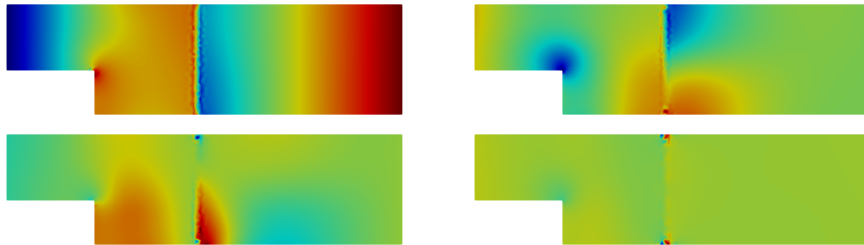


Figure 8: The first POD modes for the pressures p_1 and p_2 (subdomain functions are glued together for visualisation purposes).



Figure 9: The first POD modes for the adjoint velocities ξ_1 and ξ_2 (subdomain functions are glued together for visualisation purposes).

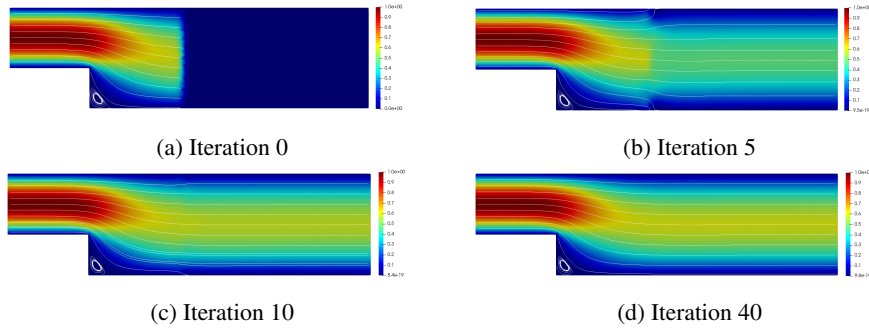


Figure 10: High-fidelity solution for the velocities u_1 and u_2 . Values of the parameters $U_{in} = 1$ and $\nu = 1$

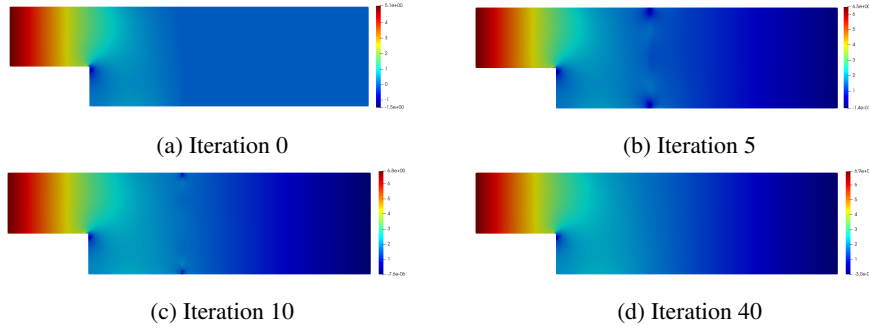


Figure 11: High-fidelity solution for the pressures p_1 and p_2 . Values of the parameters $U_{in} = 1$ and $\nu = 1$

and the resulting figures are obtained by gluing the subdomain function just for the sake of visualisation. Figure 6 shows the first modes for the fluid velocities u_1 and u_2 : in particular, notice that the modes corresponding to u_1 (on the left section of the domain) are zero at the inlet boundary due to the use of lifting function. In Figure 7 we can see the first four modes for s_1 and s_2 : here the corresponding functions are mostly localised inside the domains Ω_1 and Ω_2 thanks to the homogeneous conditions at the boundaries and the non-zero forcing term coming from the pressure. Figure 8 represents the first modes for the pressures p_1 and p_2 : we point out the signs of the oscillation behaviour which suggests that the supremiser enrichment might be needed to assure stability of the reduced-order solution. Finally, Figure 9 shows the first four modes for the adjoint variables ξ_1 and ξ_2 : note that they are concentrated only around the interface Γ_0 which is due to the fact that the only nonzero contribution in the adjoint equations is coming from the source terms which are defined solely on the interface Γ_0 .

Figures 10-13 represent the high-fidelity solutions for two different values of the parameters $(U_{in}, \nu) = (1, 1)$ and $(U_{in}, \nu) = (4.5, 0.7)$. The solutions were obtained by carrying out 40 optimisation iterations via L-BFGS-B algorithm. Figures 10 and 12 show the intermediate solutions at iteration 0, 5, 10 and 40 for the fluid velocities u_1 and u_2 , whereas Figures 11 and 13 show the corresponding pressures p_1 and p_2 . The final solution is taken to be the 40th iteration optimisation solution in which we can observe a continuity between subdomain solutions at the

Iteration	Functional Value	Gradient norm
0	$4.8 \cdot 10^{-1}$	$4.1 \cdot 10^{-1}$
5	$6.4 \cdot 10^{-2}$	$2.2 \cdot 10^{-1}$
10	$6.1 \cdot 10^{-3}$	$3.7 \cdot 10^{-2}$
40	$3.1 \cdot 10^{-5}$	$1.0 \cdot 10^{-3}$

Table 2: Functional values and the gradient norm for the optimisation solution at the parameter values $U_{in} = 1$ and $\nu = 1$

Iteration	Abs. error u_h		Rel. error u_h		Abs. error p_h		Rel. error p_h	
	Ω_1	Ω_2	Ω_1	Ω_2	Ω_1	Ω_2	Ω_1	Ω_2
0	0.03	2.99	0.09	-	10.65	7.07	0.55	-
5	0.10	0.65	0.03	0.22	2.54	1.59	0.12	0.23
10	0.03	0.11	0.008	0.03	0.44	0.29	0.02	0.04
40	0.001	0.003	0.0004	0.0009	0.015	0.012	0.0007	0.002

Table 3: Absolute and relative errors of the optimisation solution with respect to the monolithic solution at the parameter values $U_{in} = 1$ and $\nu = 1$

interface Γ_0 , see Figures 10d, 11d and Figures 12d, 13d. Moreover, it can be noticed that the solution for parameters $(U_{in}, \nu) = (1, 1)$ looks continuous already at iteration 10, which suggests that the convergence of the optimisation algorithm might depend on the Reynolds number.

We present additional details in Tables 2 - 5. In particular, in Tables 2 and 4, we list the values for the functional \mathcal{J}_γ and the $L^2(\Gamma_0)$ -norm of the gradient $\frac{d\mathcal{J}_\gamma}{dg}$ at the different iteration of the optimisation procedure, while Table 3 contains the absolute and relative errors with respect to the monolithic (entire-domain) solutions u_h, p_h , i.e.,

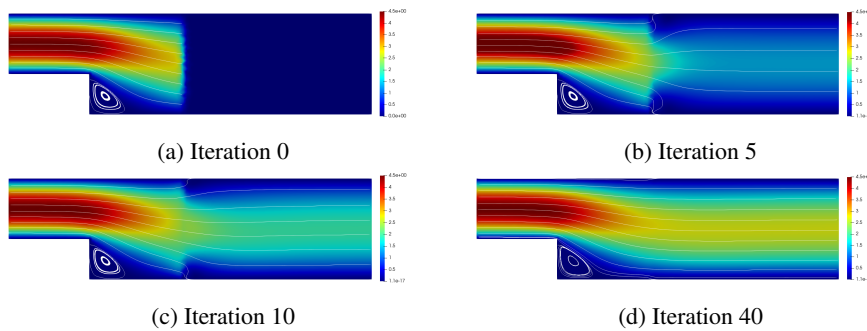


Figure 12: High-fidelity solution for the velocities u_1 and u_2 . Values of the parameters $U_{in} = 4.5$ and $\nu = 0.7$

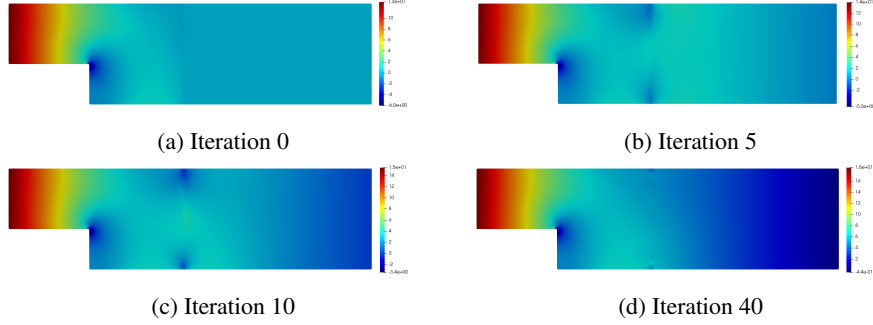


Figure 13: High-fidelity solution for the pressures p_1 and p_2 . Values of the parameters $U_{in} = 4.5$ and $\nu = 0.7$

Iteration	Functional Value	Gradient norm
0	10.09	2.71
5	3.47	2.19
10	1.77	1.46
40	0.02	0.08

Table 4: Functional values and the gradient norm for the optimisation solution at parameter values $U_{in} = 4.5$ and $\nu = 0.7$

Iteration	Abs. error u_h		Rel. error u_h		Abs. error p_h		Rel. error p_h	
	Ω_1	Ω_2	Ω_1	Ω_2	Ω_1	Ω_2	Ω_1	Ω_2
0	0.32	13.49	0.02	-	32.91	22.17	0.61	-
5	0.60	7.75	0.04	0.50	26.89	12.63	0.49	0.57
10	0.70	3.94	0.05	0.29	18.00	8.18	0.33	0.36
40	0.04	0.05	0.0003	0.003	0.32	0.22	0.006	0.01

Table 5: Absolute and relative errors of the optimisation solution with respect to the monolithic solution at the parameter values $U_{in} = 4.5$ and $\nu = 0.7$

Iteration	Functional Value	Gradient norm
0	$4.8 \cdot 10^{-1}$	0.405
5	$3.6 \cdot 10^{-3}$	0.023
10	$1.1 \cdot 10^{-3}$	0.028

Table 6: Functional values and the gradient norm for the reduced optimisation solution at parameter values $U_{in} = 1$ and $\nu = 1$

Iteration	Abs. error u_N		Rel. error u_N		Abs. error p_N		Rel. error p_N	
	Ω_1	Ω_2	Ω_1	Ω_2	Ω_1	Ω_2	Ω_1	Ω_2
0	0.03	2.99	0.007	-	1.14	7.07	0.075	-
5	0.03	0.08	0.008	0.03	0.56	0.23	0.030	0.03
10	0.001	0.028	0.003	0.009	0.092	0.089	0.004	0.01

Table 7: Absolute and relative errors of the optimisation solution with respect to the monolithic solution at the parameter values $U_{in} = 1$ and $\nu = 1$

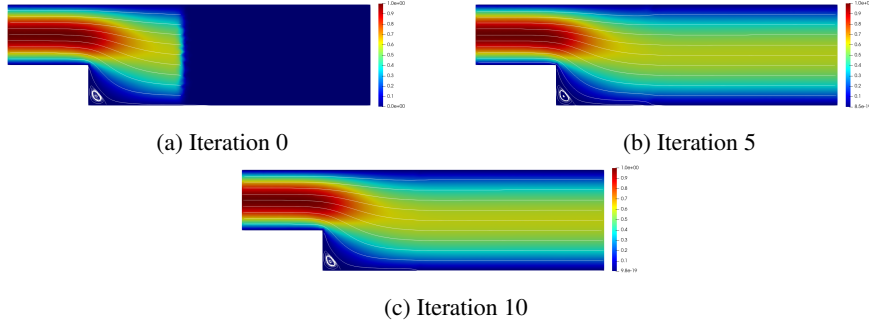


Figure 14: Reduced-order solution for the velocities u_1 and u_2 . Values of the parameters $U_{in} = 1$ and $\nu = 1$

$$\begin{aligned}
\text{Abs. error } u_h &:= \|u_{i,h} - u_h\|_{L^2(\Omega_i)} && \text{on domain } \Omega_i, \\
\text{Rel. error } u_h &:= \frac{\|u_{i,h} - u_h\|_{L^2(\Omega_i)}}{\|u_h\|_{L^2(\Omega_i)}} && \text{on domain } \Omega_i, \\
\text{Abs. error } p_h &:= \|p_{i,h} - p_h\|_{L^2(\Omega_i)} && \text{on domain } \Omega_i, \\
\text{Rel. error } p_h &:= \frac{\|p_{i,h} - p_h\|_{L^2(\Omega_i)}}{\|p_h\|_{L^2(\Omega_i)}} && \text{on domain } \Omega_i,
\end{aligned}$$

for $i = 1, 2$.

Figures 14 – 17 represent the reduced-order solutions for two different values of the parameters $(U_{in}, \nu) = (1, 1)$ and $(U_{in}, \nu) = (4, 0.75)$. In each of the cases, we choose the following number of the reduced basis functions: $N_{u_1} = N_{s_1} = N_{p_1} = N_{u_2} = N_{s_2} = N_{p_2} = N_g = 10$ and $N_{\xi_1} = N_{\xi_2} = 30$. As was previously anticipated, we use a higher number for the adjoint variables ξ_1 and ξ_2 since they show much slower decay of the singular values (see Figure 5a). The solutions were obtained by carrying out 10 optimisation iterations of L–BFGS–B algorithm. Figures 14 and 16 show the intermediate solutions at iteration 0, 5 and 10 for the fluid velocities u_1 and u_2 , whereas Figures 15 and 17 show the corresponding pressures p_1 and p_2 . The final solution, at the 10th iteration, shows continuity between subdomain solutions at the interface Γ_0 , see Figures 14c, 15c and Figures 16c, 17c.

We present additional details in Tables 6 - 9. In particular, in Tables 6 and 8, we list the values for the functional \mathcal{J}_γ and the $L^2(\Gamma_0)$ -norm of the gradient $\frac{d\mathcal{J}_\gamma}{dg}$ at the different iteration of the optimisation procedure, while Table 7 and Table 9 contain the absolute and relative errors

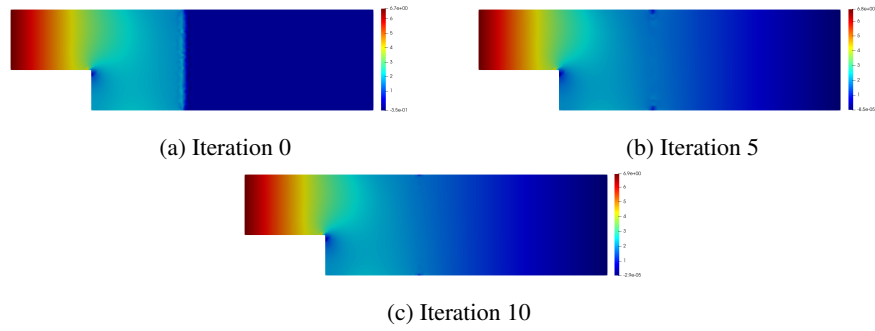


Figure 15: Reduced-order solution for the pressures p_1 and p_2 . Values of the parameters $U_{in} = 1$ and $\nu = 1$

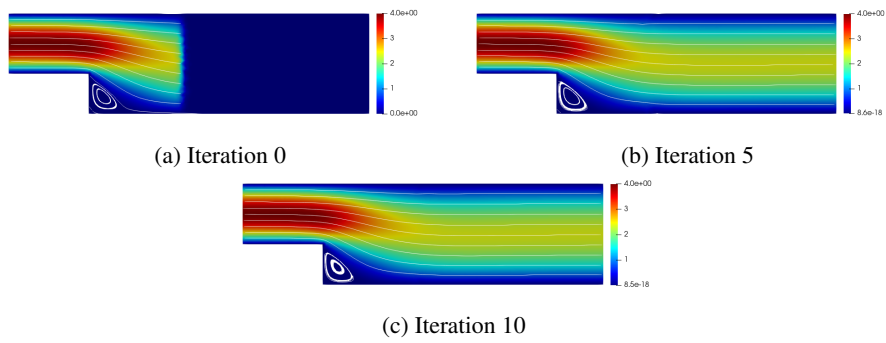


Figure 16: Reduced-order solution for the velocities u_1 and u_2 . Values of the parameters $U_{in} = 4$ and $\nu = 0.75$

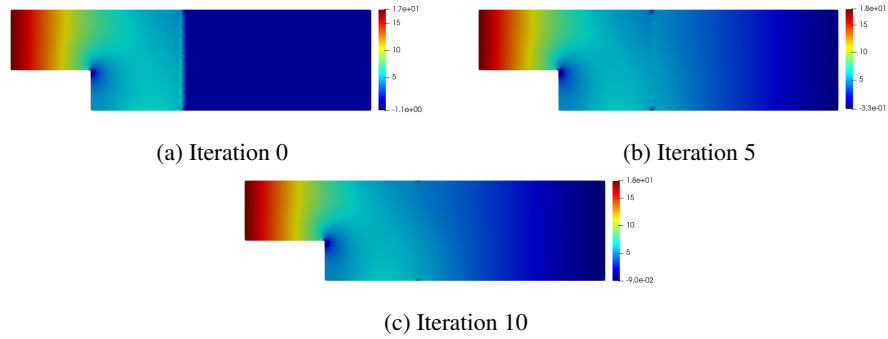


Figure 17: Reduced-order solution for the pressures p_1 and p_2 . Values of the parameters $U_{in} = 4$ and $\nu = 0.75$

Iteration	Functional Value	Gradient norm
0	7.84	2.21
5	0.043	0.21
10	0.018	0.47

Table 8: Functional values and the gradient norm for the reduced optimisation solution at parameter values $U_{in} = 4$ and $\nu = 0.75$

with respect to the monolithic (entire-domain) solutions u_h, p_h , i.e.

$$\begin{aligned}
 \text{Abs. error } u_N &:= \|u_{i,N} - u_h\|_{L^2(\Omega_i)} && \text{on domain } \Omega_i, \\
 \text{Rel. error } u_N &:= \frac{\|u_{i,N} - u_h\|_{L^2(\Omega_i)}}{\|u_h\|_{L^2(\Omega_i)}} && \text{on domain } \Omega_i, \\
 \text{Abs. error } p_N &:= \|p_{i,N} - p_h\|_{L^2(\Omega_i)} && \text{on domain } \Omega_i, \\
 \text{Rel. error } p_N &:= \frac{\|p_{i,N} - p_h\|_{L^2(\Omega_i)}}{\|p_h\|_{L^2(\Omega_i)}} && \text{on domain } \Omega_i,
 \end{aligned}$$

for $i = 1, 2$.

Analysing the results, we are able to see that the reduced basis method gives us a solution as accurate as the high-fidelity one - in both cases the relative error reported in the corresponding

Iteration	Abs. error u_N		Rel. error u_N		Abs. error p_N		Rel. error p_N	
	Ω_1	Ω_2	Ω_1	Ω_2	Ω_1	Ω_2	Ω_1	Ω_2
0	0.15	11.98	0.011	-	3.95	21.16	0.073	-
5	0.088	0.118	0.006	0.010	1.74	0.438	0.032	0.021
10	0.036	0.108	0.003	0.009	0.291	0.286	0.005	0.014

Table 9: Absolute and relative errors of the optimisation solution with respect to the monolithic solution at the parameter values $U_{in} = 4$ and $\nu = 0.75$

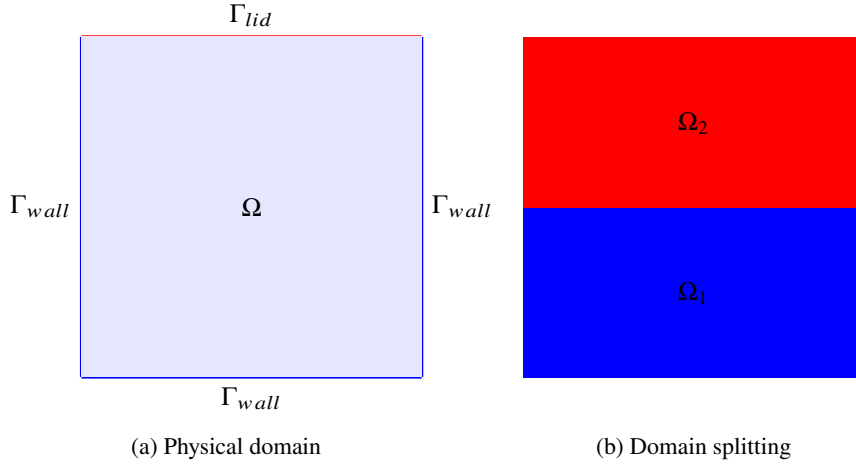


Figure 18: Lid-driven cavity flow geometry

tables is less than 1%. The reduced-order approximation of the optimisation problem at hand allowed us to reduce the dimension of the high-fidelity optimisation functional by more than 10 times and enabled us to use 4 times fewer iterations in the optimisation algorithm (each optimisation step requires at least one solve of the state and the adjoint equations). We also note that the fact that we chose a bigger number of the reduced basis functions for the adjoint variables ξ_1 and ξ_2 is not supposed to affect the computational costs much, since the adjoint problem is linear and does not require multiple Newton iteration to be solved so that the biggest computational effort still lies in the nonlinear Navier–Stokes equations and the optimisation process.

6.2 Lid-driven cavity flow test case

In this section, we provide the numerical simulation for the lid-driven cavity flow test case. Figure 18a represents the physical domain of interest - the unit square. The split into two domains is performed by dissecting the domain by a median horizontal line as shown in Figure 18b.

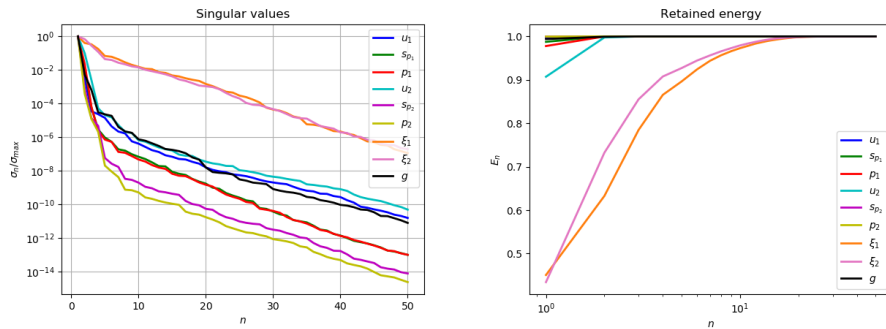
We impose homogeneous Dirichlet boundary conditions on the part of the boundary Γ_{wall} for the fluid velocity and the nonzero horizontal constant velocity on the lid boundary Γ_{lid} : $u_{lid} = (\bar{U}, 0)$; the values of \bar{U} are reported in Table 10.

Two physical parameters are considered: viscosity ν and the magnitude \bar{U} of the lid velocity profile u_{in} . Details of the offline stage and the finite-element discretisation are summarised in Table 10. High-fidelity solutions are obtained by carrying out the minimisation in the space of dimension equal to the number of degrees of freedom at the interface, which is 138 in our test case. The best performance has been achieved by using the limited-memory Broyden–Fletcher–Goldfarb–Shanno (L-BFGS-B) optimisation algorithm, and two stopping criteria are applied: either the maximal number of iteration It_{max} is reached or the gradient norm of the target functional is less than the given tolerance Tol_{opt} .

Snapshots are sampled from a training set of M parameters uniformly sampled in the 2-dimensional parameter space, and the first N_{max} POD modes have been retained. Figure 19a shows POD singular values for all the state, the adjoint and the control variables. As it can be seen, the POD singular values corresponding to the adjoint velocities ξ_1 and ξ_2 feature a slower

Physical parameters	2 : ν, \bar{U}
Range ν	[0.05, 2]
Range \bar{U}	[0.5, 5]
FE velocity order	2
FE pressure order	1
Total number of FE dofs	14,867
Number of FE dofs at the interface	138
Optimisation algorithm	L-BFGS-B
It_{max}	40
Tol_{opt}	10^{-5}
M	760
N_{max}	50

Table 10: Computational details of the offline stage.



(a) POD singular values as a function of number n of POD modes (log scaling in y -direction) (b) Energy retained by the first N_{max} POD modes (log scaling in x -direction)

Figure 19: Results of the offline stage: POD singular eigenvalue decay (a) and retained energy (b) of the the first N_{max} POD modes

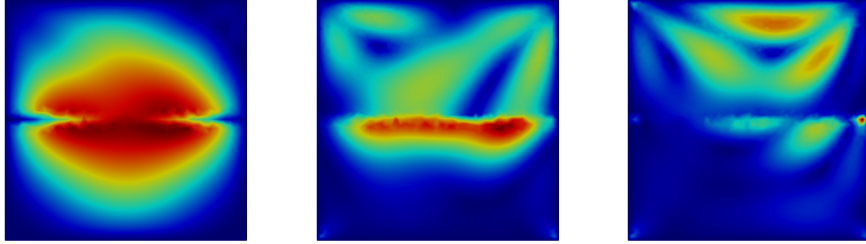


Figure 20: The first POD modes for the velocities u_1 and u_2 (subdomain functions are glued together for visualisation purposes).

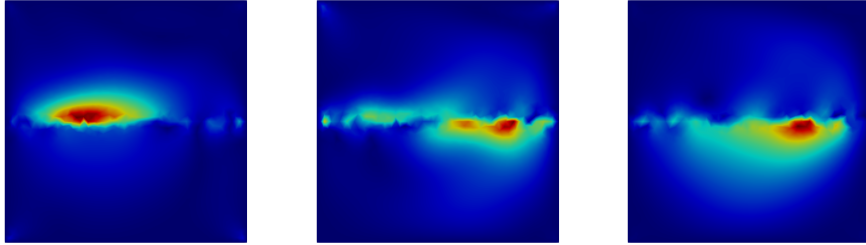


Figure 21: The first POD modes for the adjoint velocities ξ_1 and ξ_2 (subdomain functions are glued together for visualisation purposes).

decay compared to the one for the other variables. In Figure 19b, we can see the behaviour of the energy E_n retained by the first N modes for different components of the solution. Note that as it was in the previous numerical case, the highest number of modes is needed to correctly represent the adjoint variables ξ_1 and ξ_2 .

Figures 20–21 represent first three POD modes for the variables u_1, u_2 and ξ_1, ξ_2 . We stress that the POD modes were obtained separately for each component and the resulting figures are obtained by glueing the subdomain function just for the sake of visualisation.

Figure 20 shows the first modes for the fluid velocities u_1 and u_2 : in particular, notice that the modes corresponding to u_2 (on the upper section of the domain) are zero at the lid boundary due to the use of lifting function. Figure 21 shows the first three modes for the adjoint variables ξ_1 and ξ_2 : note that they are concentrated only around the interface Γ_0 which is due to the fact that the only nonzero contribution in the adjoint equations is coming from the source terms which are defined solely on the interface Γ_0 .

Figures 22 and 23 represent the high-fidelity solutions for two different values of the parameters $(U_{in}, \nu) = (5, 0.05)$ and $(U_{in}, \nu) = (1, 0.1)$. The solutions were obtained by carrying out 25 optimisation iterations via L-BFGS-B algorithm. Figures 22 and 23 show the intermediate solutions at iteration 0, 5 and 25 for the fluid velocities u_1 and u_2 . The final solution is taken to be the 25-iteration optimisation solution as we can observe a continuity between subdomain solutions at the interface Γ_0 .

We present additional details in Tables 11 - 14. In particular, in Tables 11 and 13, we list the values for the functional \mathcal{J}_γ and the $L^2(\Gamma_0)$ -norm of the gradient $\frac{d\mathcal{J}_\gamma}{dg}$ at the different iteration of the optimisation procedure, while Table 12 and Table 14 contain the absolute and relative errors with respect to the monolithic(entire-domain) solutions u_h, p_h .

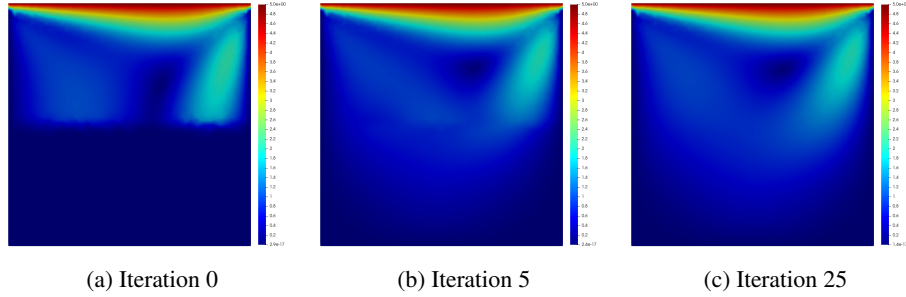


Figure 22: High-fidelity solution for the velocities u_1 and u_2 . Values of the parameters $U_{in} = 5$ and $\nu = 0.05$

Iteration	Functional Value	Gradient norm
0	$4.4 \cdot 10^{-1}$	3.398
5	$3.0 \cdot 10^{-2}$	1.001
10	$3.5 \cdot 10^{-3}$	0.171
25	$8.7 \cdot 10^{-5}$	0.016

Table 11: Functional values and the gradient norm for the optimisation solution at parameter values $U_{in} = 5$ and $\nu = 0.05$

Iteration	Rel. error u_h		Rel. error p_h	
	Ω_1	Ω_2	Ω_1	Ω_2
0	-	0.165	-	0.013
5	0.183	0.052	0.051	0.002
10	0.033	0.012	0.017	0.0009
25	0.015	0.005	0.014	0.0006

Table 12: Relative errors of the optimisation solution with respect to the monolithic solution at the parameter values $U_{in} = 5$ and $\nu = 0.05$

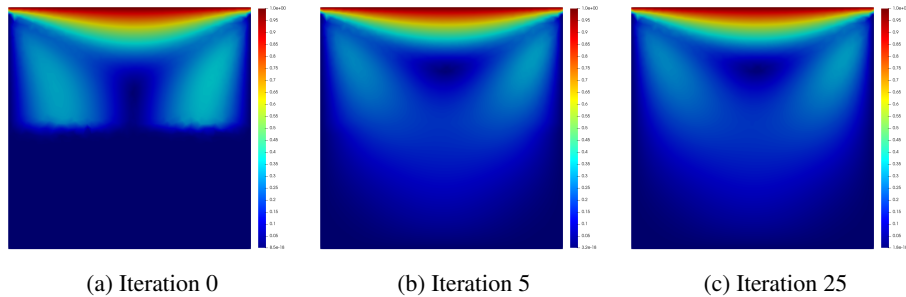


Figure 23: High-fidelity solution for the velocities u_1 and u_2 . Values of the parameters $U_{in} = 1$ and $\nu = 0.1$

Iteration	Functional Value	Gradient norm
0	$2.5 \cdot 10^{-2}$	$4.1 \cdot 10^{-1}$
5	$7.4 \cdot 10^{-5}$	$1.4 \cdot 10^{-2}$
10	$3.3 \cdot 10^{-6}$	$9.1 \cdot 10^{-4}$
25	$7.0 \cdot 10^{-7}$	$3.9 \cdot 10^{-4}$

Table 13: Functional values and the gradient norm for the optimisation solution at the parameter values $U_{in} = 1$ and $\nu = 0.1$

Iteration	Rel. error u_h		Rel. error p_h	
	Ω_1	Ω_2	Ω_1	Ω_2
0	-	-	0.242	0.05
5	0.048	0.015	0.011	0.0004
10	0.0001	0.010	0.003	0.0003
25	0.0007	0.009	0.002	0.0003

Table 14: Relative errors of the optimisation solution with respect to the monolithic solution at the parameter values $U_{in} = 1$ and $\nu = 0.1$

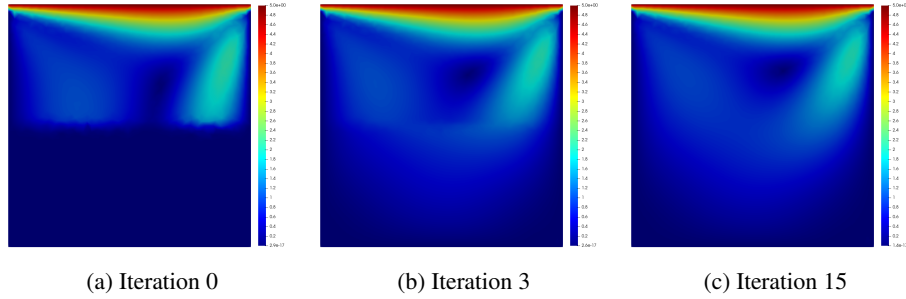


Figure 24: Reduced-order solution for the velocities u_1 and u_2 . Values of the parameters $U_{in} = 5$ and $\nu = 0.05$

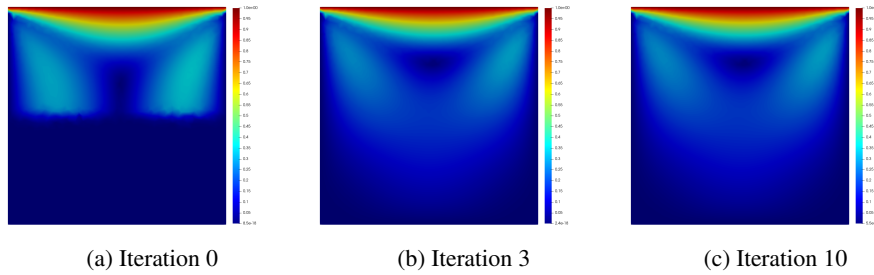


Figure 25: Reduced-order solution for the velocities u_1 and u_2 . Values of the parameters $U_{in} = 1$ and $\nu = 0.1$

Iteration	Functional Value	Gradient norm
0	$4.4 \cdot 10^{-1}$	3.398
3	$1.9 \cdot 10^{-2}$	6.062
6	$1.6 \cdot 10^{-3}$	0.550
15	$8.0 \cdot 10^{-5}$	0.157

Table 15: Functional values and the gradient norm for the reduced optimisation solution at parameter values $U_{in} = 5$ and $\nu = 0.05$

Iteration	Rel. error u_N		Rel. error p_N	
	Ω_1	Ω_2	Ω_1	Ω_2
0	-	0.165	-	0.013
3	0.078	0.052	0.037	0.002
6	0.040	0.020	0.018	0.0008
15	0.013	0.004	0.013	0.0005

Table 16: Relative errors of the reduced optimisation solution with respect to the monolithic solution at the parameter values $U_{in} = 5$ and $\nu = 0.05$

Figures 24 – 25 represent the reduced-order solutions for two different values of the parameters $(U_{in}, \nu) = (5, 0.05)$ and $(U_{in}, \nu) = (1, 0.1)$. For the case $(U_{in}, \nu) = (5, 0.05)$ we choose the following number of the reduced basis functions: $N_{u_1} = N_{s_1} = N_{p_1} = N_{u_2} = N_{s_2} = N_{p_2} = N_g = 10$, where for the case $(U_{in}, \nu) = (1, 0.1)$ we chose $N_{u_1} = N_{s_1} = N_{p_1} = N_{u_2} = N_{s_2} = N_{p_2} = N_g = 5$; in either of cases we fixed $N_{\xi_1} = N_{\xi_2} = 15$. As it was mentioned before we use a higher number for the adjoint variables ξ_1 and ξ_2 since they show much slower decay of the singular values (see Figure 19a). Figure 24 shows the intermediate solutions at iteration 0, 3 and 15 for the fluid velocities u_1 and u_2 corresponding to the parameter value $(U_{in}, \nu) = (5, 0.05)$, and Figure 25 shows the velocities u_1 and u_2 for the parameter value $(U_{in}, \nu) = (1, 0.1)$. The final solutions are taken to be the 15-iteration optimisation solution in the former case and the 10-iteration optimisation solution in the latter.

We present additional details in Tables 15 - 18. In particular, in Tables 15 and 17 we list the values for the functional \mathcal{J}_y and the $L^2(\Gamma_0)$ -norm of the gradient $\frac{d\mathcal{J}_y}{dg}$ at the different iteration of the optimisation procedure, while Table 16 and Table 18 contain the L^2 -relative errors with respect to the monolithic (the entire-domain) solutions u_h, p_h .

Analyzing the results, we are able to see that the reduced basis method gives us a solution as accurate as the high-fidelity modes - in both cases the relative error reported in the corresponding

Iteration	Functional Value	Gradient norm
0	$2.5 \cdot 10^{-2}$	$4.1 \cdot 10^{-1}$
3	$9.1 \cdot 10^{-6}$	$1.0 \cdot 10^{-2}$
6	$7.3 \cdot 10^{-7}$	$2.8 \cdot 10^{-3}$
10	$2.4 \cdot 10^{-7}$	$2.7 \cdot 10^{-3}$

Table 17: Functional values and the gradient norm for the reduced optimisation solution at the parameter values $U_{in} = 1$ and $\nu = 0.1$

Iteration	Rel. error u_N		Rel. error p_N	
	Ω_1	Ω_2	Ω_1	Ω_2
0	-	0.242	-	0.005
3	0.018	0.002	0.008	0.003
6	0.006	0.001	0.006	0.002
10	0.003	0.001	0.005	0.001

Table 18: Absolute and relative errors of the reduced optimisation solution with respect to the monolithic solution at the parameter values $U_{in} = 1$ and $\nu = 0.1$

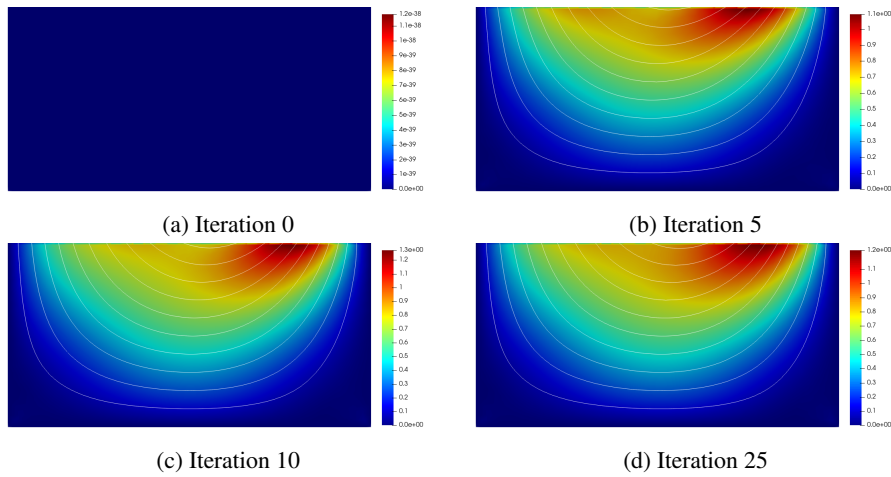


Figure 26: Reduced-order solution for the velocity u_1 . Values of the parameters $U_{in} = 5$ and $\nu = 0.05$

tables is less than 1 – 2%. The reduced-order approximation of the optimisation problem at hand allowed us to reduce the dimension of the high-fidelity optimisation functional by more than 10-20 times and enabled us to use half optimisation algorithm iterations (each optimisation step requires at least one solve of the state and the adjoint equations).

In order to provide more visually representable results (the scale of the solution on the subdomains Ω_1 and Ω_2 has a few orders of the difference in the magnitude), we provide the graphs of the velocities u_1 and u_2 separately in Figures 26 and 27.

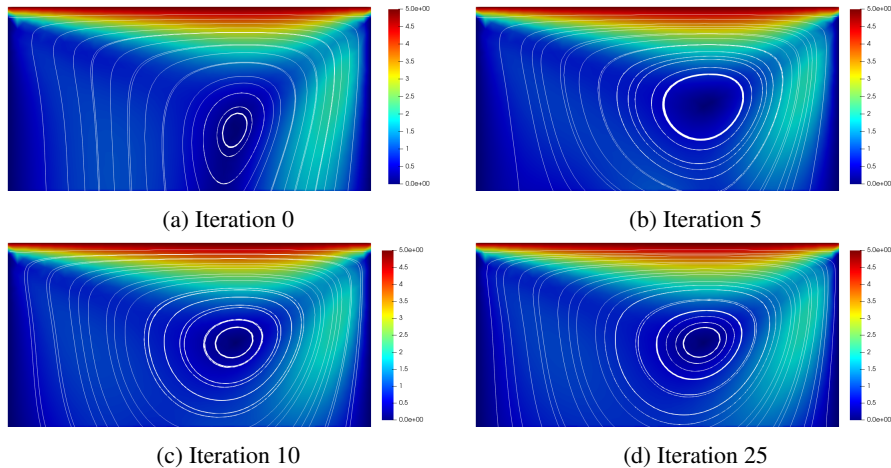


Figure 27: Reduced-order solution for the velocity u_2 . Values of the parameters $U_{in} = 5$ and $\nu = 0.05$

7 Conclusions

In this work, we proposed a reduced-order model for the optimisation-based domain decomposition formulation of the parameter-dependent stationary incompressible Navier-Stokes equations.

The original problem cast into the optimisation-based domain-decomposition framework leads to the optimal control problem aimed at minimising the coupling error at the interface; the problem, then, has been tackled using an iterative gradient-based optimisation algorithm, which allowed us to obtain a complete separation of the solvers on different subdomains.

On the reduced-order level, we have managed to build a model for which the generation of the reduced basis spaces is carried out separately in each subdomain and for each component of the problem solution. Furthermore, as the numerical results show, the reduction of the optimal-control problem can be observed not only in the dimensions of the different components of the problem, i.e., of the functional, the state and the adjoint equations but also in the number of the iterations of the optimisation algorithm.

As it has been mentioned in the paper, the aforementioned techniques could be promising in the context of more complex time-dependent problems and, more importantly, multi-physics problems, where either pre-existing solvers can be used on each subcomponent or we do not have direct access to the codes. In particular, in future, we are planning to extend the methodology presented in this paper to the nonstationary fluid-dynamics problems and, eventually, to Fluid-Structure interaction problems. Moreover, this approach can be applied also to more complicated problems, where different types of numerical models are used in different subdomains.

Acknowledgements

This work was supported by the European Union's Horizon 2020 research and innovation programme under the Marie Skłodowska-Curie Actions [grant agreement 872442] (ARIA, Accurate Roms for Industrial Applications) and by PRIN "Numerical Analysis for Full and Reduced Order Methods for Partial Differential Equations" (NA-FROM-PDEs) project. MN acknowledges the

support of the Austrian Science Fund (FWF) project F65 “Taming complexity in Partial Differential Systems” and the Austrian Science Fund (FWF) project P 33477. DT has been funded by a SISSA Mathematical fellowship within Italian Excellence Departments initiative by Ministry of University and Research. FB also thanks the project “Reduced order modelling for numerical simulation of partial differential equations” funded by Università Cattolica del Sacro Cuore.

References

- [1] multiphenics - easy prototyping of multiphysics problems in FEniCS, <http://mathlab.sissa.it/multiphenics>, 2016.
- [2] RBniCS - reduced order modelling in FEniCS, <http://mathlab.sissa.it/rbnics>, 2015.
- [3] S. Ali, F. Ballarin, and G. Rozza. Stabilized reduced basis methods for parametrized steady Stokes and Navier–Stokes equations. *Computers & Mathematics with Applications*, 80(11):2399–2416, 2020. High-Order Finite Element and Isogeometric Methods 2019.
- [4] M. Astorino, F. Chouly, and M. A. Fernández. Robin Based Semi-Implicit Coupling in Fluid-Structure Interaction: Stability Analysis and Numerics. *SIAM Journal on Scientific Computing*, 31(6):4041–4065, 2010.
- [5] F. Ballarin, A. Manzoni, A. Quarteroni, and G. Rozza. Supremizer stabilization of POD–Galerkin approximation of parametrized steady incompressible Navier–Stokes equations. *International Journal for Numerical Methods in Engineering*, 102(5):1136–1161, 2015.
- [6] F. Ballarin and G. Rozza. POD–Galerkin monolithic reduced order models for parametrized fluid-structure interaction problems. *International Journal for Numerical Methods in Fluids*, 82(12):1010–1034, 2016.
- [7] F. Ballarin, G. Rozza, and Y. Maday. Reduced-order semi-implicit schemes for fluid-structure interaction problems. In *Model Reduction of Parametrized Systems*, pages 149–167. Springer, 2017.
- [8] M. Benzi, G. H. Golub, and J. Liesen. Numerical solution of saddle point problems. *Acta Numerica*, 14:1–137, 2005.
- [9] G. Carere, M. Strazzullo, F. Ballarin, G. Rozza, and R. Stevenson. A weighted POD-reduction approach for parametrized PDE-constrained Optimal Control Problems with random inputs and applications to environmental sciences. *Computers & Mathematics with Applications*, 102:261–276, 2021.
- [10] P. Causin, J. Gerbeau, and F. Nobile. Added-mass effect in the design of partitioned algorithms for fluid–structure problems. *Computer Methods in Applied Mechanics and Engineering*, 194(42):4506–4527, 2005.
- [11] R. Crisovan, D. Torlo, R. Abgrall, and S. Tokareva. Model order reduction for parametrized nonlinear hyperbolic problems as an application to uncertainty quantification. *Journal of Computational and Applied Mathematics*, 348:466–489, 2019.
- [12] A. de Castro, P. Kuberry, I. Tezaur, and P. Bochev. A novel partitioned approach for reduced order model – Finite Element model (ROM-FEM) and ROM-ROM coupling, 2022.
- [13] S. Debaris and G. Rozza. Reduced basis method for multi-parameter-dependent steady Navier-Stokes equations: Applications to natural convection in a cavity. *Journal of Computational Physics*, 228(12):4359–4378, 2009.
- [14] V. Ervin, E. Jenkins, and H. Lee. Approximation of the Stokes–Darcy system by optimization. *Journal of Scientific Computing*, 59, 06 2014.

- [15] A.-L. Gerner and K. Veroy. Certified reduced basis methods for parametrized saddle point problems. *SIAM Journal on Scientific Computing*, 34(5):A2812–A2836, 2012.
- [16] P. Gosselet, V. Chiaruttini, C. Rey, and F. Feyel. A monolithic strategy based on an hybrid domain decomposition method for multiphysic problems. application to poroelasticity. *Revue Européenne des Éléments Finis*, 13, 04 2012.
- [17] M. Gunzburger and H. K. Lee. A domain decomposition method for optimization problems for partial differential equations. *Computers & Mathematics with Applications*, 40(2):177–192, 2000.
- [18] M. Gunzburger, J. Peterson, and H. Kwon. An optimization based domain decomposition method for partial differential equations. *Computers & Mathematics with Applications*, 37(10):77–93, 1999.
- [19] M. D. Gunzburger. *Perspectives in Flow Control and Optimization*. Society for Industrial and Applied Mathematics, 2002.
- [20] M. D. Gunzburger and H. K. Lee. An optimization-based domain decomposition method for the Navier–Stokes equations. *SIAM Journal on Numerical Analysis*, 37(5):1455–1480, 2000.
- [21] B. Haasdonk. *Reduced Basis Methods for Parametrized PDEs—A Tutorial Introduction for Stationary and Instationary Problems*, chapter 2, pages 65–136. Society for Industrial and Applied Mathematics, 2017.
- [22] J. S. Hesthaven, G. Rozza, and B. Stamm. *Certified Reduced Basis Methods for Parametrized Partial Differential Equations*. Springer Briefs in Mathematics. Springer, Switzerland, 1 edition, 2015.
- [23] M. Hinze, R. Pinnau, M. Ulbrich, and S. Ulbrich. *Optimization with PDE Constraints*, volume 23 of *Mathematical modelling*. Springer, 2009.
- [24] T. T. P. Hoang and H. Lee. A global-in-time domain decomposition method for the coupled nonlinear Stokes and Darcy flows. *Journal of Scientific Computing*, 87, 04 2021.
- [25] P. Kuberry and H. K. Lee. A decoupling algorithm for fluid-structure interaction problems based on optimization. *Computer Methods in Applied Mechanics and Engineering*, 267:594–605, 2013.
- [26] P. Kuberry and H. K. Lee. Analysis of a fluid-structure interaction problem recast in an optimal control setting. *SIAM Journal on Numerical Analysis*, 53(3):1464–1487, 2015.
- [27] J. E. Lagnese, G. Leugering, and G. Leugering. *Domain in Decomposition Methods in Optimal Control of Partial Differential Equations*. Number 148 in International Series of Numerical Mathematics. Springer Science & Business Media, 2004.
- [28] T. Lassila, A. Manzoni, A. Quarteroni, and G. Rozza. Model order reduction in fluid dynamics: challenges and perspectives. In A. Quarteroni and G. Rozza, editors, *Reduced Order Methods for Modeling and Computational Reduction*, volume 9, pages 235–274. Springer MS&A Series, 2014.
- [29] M. Nonino, F. Ballarin, and G. Rozza. A monolithic and a partitioned reduced basis method for fluid–structure interaction problems. *Fluids*, 6(6), 2021.
- [30] M. Nonino, F. Ballarin, G. Rozza, and Y. Maday. Projection based semi–implicit partitioned reduced basis method for non parametrized and parametrized Fluid–Structure Interaction problems. *arXiv preprint arXiv:2201.03236*, 2022.
- [31] A. Quarteroni and A. Valli. *Numerical Approximation of Partial Differential Equations*. Springer Series in Computational Mathematics. 23. Springer Berlin Heidelberg, Heidelberg, DE, 1994. Written for: Numerical analysts, applied mathematicians.

- [32] A. Quarteroni and A. Valli. *Domain decomposition Methods for Partial Differential Equations*. Oxford University Press, Oxford, UK, 1999.
- [33] G. Rozza. Reduced basis methods for stokes equations in domains with non-affine parameter dependence. *Computing and Visualization in Science*, 12:23–35, 2009.
- [34] G. Rozza, D. Huynh, and A. Patera. Reduced basis approximation and a posteriori error estimation for affinely parametrized elliptic coercive partial differential equations. *Archives of Computational Methods in Engineering*, 15:1–47, 09 2007.
- [35] G. Stabile, F. Ballarin, G. Zuccarino, and G. Rozza. A reduced order variational multiscale approach for turbulent flows. *Advances in Computational Mathematics*, 45(5):2349–2368, 2019.
- [36] G. Stabile and G. Rozza. Finite volume POD-Galerkin stabilised reduced order methods for the parametrised incompressible Navier–Stokes equations. *Computers & Fluids*, 173:273–284, 2018.
- [37] M. Strazzullo, F. Ballarin, and G. Rozza. POD–Galerkin model order reduction for parametrized time dependent linear quadratic optimal control problems in saddle point formulation. *Journal of Scientific Computing*, 83(3):1–35, 2020.
- [38] M. Strazzullo, M. Girfoglio, F. Ballarin, T. Iliescu, and G. Rozza. Consistency of the full and reduced order models for evolve-filter-relax regularization of convection-dominated, marginally-resolved flows. *International Journal for Numerical Methods in Engineering*, 123(14):3148–3178, 2022.
- [39] M. Tezzele, N. Demo, G. Stabile, A. Mola, and G. Rozza. Enhancing CFD predictions in shape design problems by model and parameter space reduction. *Advanced Modeling and Simulation in Engineering Sciences*, 7(1):1–19, 2020.
- [40] D. Torlo, F. Ballarin, and G. Rozza. Stabilized weighted reduced basis methods for parametrized advection dominated problems with random inputs. *SIAM/ASA Journal on Uncertainty Quantification*, 6(4):1475–1502, 2018.
- [41] D. Torlo and M. Ricchiuto. Model order reduction strategies for weakly dispersive waves. *arXiv preprint arXiv:2112.10608*, 2021.
- [42] V. Tsiolakis, M. Giacomini, R. Sevilla, C. Othmer, and A. Huerta. Nonintrusive proper generalised decomposition for parametrised incompressible flow problems in openfoam. *Computer physics communications*, 249:107013, 2020.
- [43] L. Venturi, F. Ballarin, and G. Rozza. A weighted POD method for elliptic PDEs with random inputs. *Journal of Scientific Computing*, 81(1):136–153, 2019.